Bioactive Materials 22 (2023) 239–253

Contents lists available at ScienceDirect

Bioactive Materials

journal homepage: www.keaipublishing.com/en/journals/bioactive-materials

Tumor Microenvironment-Adaptive Nanoplatform Synergistically Enhances Cascaded Chemodynamic Therapy

Yuemin Wang [a], Duan Wang [b], Yuyue Zhang [a], Hong Xu [b], Luxuan Shen [a], Jing Cheng [a], Xinyuan Xu [a], Hong Tan [a], Xingyu Chen [a,c,**], Jianshu Li [a,d,*]

[a] College of Polymer Science and Engineering, State Key Laboratory of Polymer Materials Engineering, Sichuan University, Chengdu, 610065, China
[b] Orthopedic Research Institution, Department of Orthopedics, West China Hospital, Sichuan University, Chengdu, 610041, China
[c] College of Medicine, Southwest Jiaotong University, Chengdu, 610003, China
[d] State Key Laboratory of Oral Diseases, West China Hospital of Stomatology, Med-X Center for Materials, Sichuan University, Chengdu, 610041, China

ARTICLE INFO

Keywords:
Chemodynamic therapy
Tumor microenvironment
Cell membranes
Homologous targeting
Perfluoropentane
Glucose oxidase

ABSTRACT

Chemodynamic therapy (CDT), a noninvasive strategy, has emerged as a promising alternative to conventional chemotherapy for treating tumors. However, its therapeutic effect is limited by the amount of H_2O_2, pH value, the hypoxic environment of tumors, and it has suboptimal tumor-targeting ability. In this study, tumor cell membrane-camouflaged mesoporous Fe_3O_4 nanoparticles loaded with perfluoropentane (PFP) and glucose oxidase (GOx) are used as a tumor microenvironment-adaptive nanoplatform (M-mFeP@O_2-G), which synergistically enhances the antitumor effect of CDT. Mesoporous Fe_3O_4 nanoparticles are selected as inducers for photothermal and Fenton reactions and as nanocarriers. GOx depletes glucose within tumor cells for starving the cells, while producing H_2O_2 for subsequent ·OH generation. Moreover, PFP, which can carry O_2, relieves hypoxia in tumor cells and provides O_2 for the cascade reaction. Finally, the nanoparticles are camouflaged with osteosarcoma cell membranes, endowing the nanoparticles with homologous targeting and immune escape abilities. Both *in vivo* and *in vitro* evaluations reveal high synergistic therapeutic efficacy of M-mFeP@O_2-G, with a desirable tumor-inhibition rate (90.50%), which indicates the great potential of this platform for clinical treating cancer.

1. Introduction

Tumor development poses a great threat to human health and life, and the number of deaths caused by tumors is increasing worldwide [1,2]. Thus, there is an urgent need to develop methods for safe and effective tumor treatment [3]. At present, chemotherapy, surgery, and radiotherapy are still the main methods for treating tumors, although they have many disadvantages, such as serious side effects and increased risk of metastasis [4,5]. The tumor microenvironment (TME) is the internal environment of tumors and is characterized by low pH, H_2O_2 accumulation, hypoxia, and inflammation [6,7]. This environment not only provides conducive conditions for tumor cell growth, expansion, and metastasis but can also form the basis for the highly specific treatment of tumors [8,9]. Tumor treatment strategies targeting the TME can effectively inhibit tumor growth, providing crucial clinical benefit [10,11].

Chemodynamic therapy (CDT), an emerging noninvasive therapy, is considered less toxic and more specific than traditional tumor treatments [12,13]. CDT can kill tumor cells through Fenton/Fenton-like reactions that convert the endogenous H_2O_2 of the TME into highly toxic ·OH [14,15]. It has emerged as one of the most promising therapeutic approaches and is developing rapidly [16,17]. A variety of Fe-based Fenton reactions, including Fe_3O_4, Fe_5C_2, and Fe^{2+}-polyphenol chelates, have been widely studied for their antitumor effects *in vivo* [18,19]. Zhang et al. developed novel FeO/MoS_2 nanocomposites with enhanced CDT that can effectively inhibit the growth of tumor cells

Peer review under responsibility of KeAi Communications Co., Ltd.
* Corresponding author. College of Polymer Science and Engineering, State Key Laboratory of Polymer Materials Engineering, Sichuan University, Chengdu, 610065, China.
** Corresponding author. College of Polymer Science and Engineering, State Key Laboratory of Polymer Materials Engineering, Sichuan University, Chengdu, 610065, China.
E-mail addresses: chenxy@swjtu.edu.cn (X. Chen), jianshu_li@scu.edu.cn (J. Li).

https://doi.org/10.1016/j.bioactmat.2022.09.025
Received 30 August 2022; Received in revised form 26 September 2022; Accepted 28 September 2022

[20]. Liu et al. designed nanoparticles in which Fe^{3+} ions chelated to tannic acid spontaneously on the surface of sorafenib nanoparticles, intervening in iron metabolism to enhance CDT [21]. However, CDT is limited by low H_2O_2 concentrations, low pH values, and a hypoxic environment [22,23]. Therefore, certain strategies, such as the direct delivery of glucose oxidase (GOx) and H2O2 into tumor cells, may decrease the local pH and increase the level of H_2O_2 in tumor cells [24,25]. However, leakage during the delivery process and phagocytosis by the cells of the reticuloendothelial system are inevitable and are harmful to normal cells [26]. In addition, the catalytic efficiency of GOx depends on the local O_2 content and the catalytic temperature (43–60 °C) [27]. Therefore, exploring a TME-adaptive nanoplatform that can not only decrease the pH value and increase the concentration of O2 in tumor cells but also efficiently generate a high concentration of H_2O_2 *in situ* is needed to enhance the efficacy of CDT.

In addition, most nanoparticles for CDT lack the ability to target tumors and hence cannot effectively localize in the tumor site, limiting their therapeutic effect and causing serious toxicity and side effects [28]. Nanoparticles camouflaged with cell membranes, such as erythrocyte membranes [29,30], immune cell membranes [31], stem cell membranes [32], and tumor cell membranes [33], have attracted considerable attention because of their excellent biological properties [34,35]. In particular, decoration with tumor cell membranes can endow nanoparticles with high biocompatibility, immune escape abilities, and homologous targeting, owing to the specific membrane proteins [36–39]. Therefore, camouflaging nanoparticles with tumor cell membranes to enhance homologous targeting and the immune escape properties of nanoparticles may be a good strategy for enhancing the tumor-treating efficacy of CDT.

In this study, we selected mesoporous Fe_3O_4 (mFe_3O_4) nanoparticles with a large surface-to-volume ratio and excellent photothermal effect as inducers of Fenton reactions and nanocarriers. At the same time, GOx was encapsulated in these nanoparticles to deplete glucose in the TME and generate gluconic acid and H_2O_2 *in situ*, further enhancing the Fenton reaction and subsequently generating ·OH. Further, perfluorocarbon (PFP) with a large O2 reservation capacity was applied to provide O_2 for this cascade reaction. Finally, K7M2-WT (K7M2) osteosarcoma cell membranes were used to camouflage the nanoparticles (M-mFeP@O_2-G, Fig. 1A) and treat osteosarcoma, as tumor cell membranes have a stronger affinity to homologous tumor cells because of specific proteins on their surfaces. When these M-mFeP@O_2-G nanoparticles are injected intravenously into mice, the tumor cell membranes on the surface of these nanoparticles can direct them to accumulate at the tumor sites and then disintegrate to release Fe ions, GOx, and O_2 in the slightly acidic environment of the TME. These released substances can lead to a series of self-amplifying catalytic cascade *in situ* under 808 nm laser radiation, which can kill tumor cells *via* enhanced CDT, starvation therapy, and photothermal therapy (PTT), as shown in Fig. 1B. This new TME-adaptive nanoplatform for enhancing CDT efficacy shows promise for effectively treating tumors.

2. Results and discussion

2.1. Synthesis and characterization of M-mFeP@O_2-G nanoparticles

Tumor cell membrane-camouflaged nanoparticles were prepared, as shown in Fig. 1. First, mFe_3O_4 nanoparticles were synthesized, and scanning electron microscopy (SEM) and transmission electron microscopy (TEM) both showed that mFe_3O_4 nanoparticles had a uniform and discrete spherical morphology within nanoscale dimensions (Figs. S1A and S1B). Powder X-ray diffraction (XRD) patterns for all the mFe_3O_4 nanoparticles were also evaluated, and the characteristic diffraction peaks of all the mFe_3O_4 nanoparticles can be well indexed to the (220), (311), (400), (422), (511), and (440) planes according to JCPDS 19–0629 (Fig. S2A). Among them, the primary magnetite nanocrystals from the mFe_3O_4 nanoparticles gave rise to the strongest and sharpest X-ray diffraction peaks, indicating the formation of highly crystalline Fe_3O_4. The elemental composition of mFe_3O_4 was also analyzed *via* X-ray photoelectron spectroscopy (XPS), which confirmed the presence of Fe and O elements (Fig. S2B). In addition, Brunauer–Emmett–Teller (BET) N_2 adsorption-desorption analysis showed that the surface area and pore size of mFe_3O_4 were 162.72 m^2 g^{-1} and 18.123 nm, respectively, which belong to the range of mesoporous nanoparticles (Fig. S3) [40]. Their unique structure with a large pore size and surface area

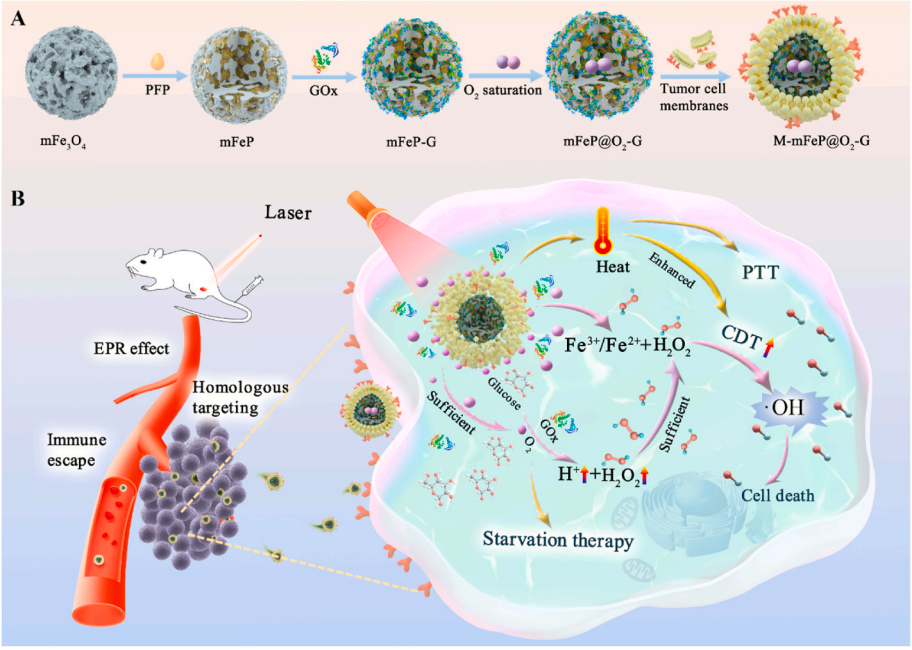

Fig. 1. Schematic of the tumor microenvironment adaptive nanoplatform for cascaded CDT for the treatment of osteosarcoma. A) Schematic illustration of the preparation of M-mFeP@O_2-G nanoparticles. B) Schematic diagram of the mechanisms of M-mFeP@O_2-G nanoparticles for tumor-specific cascade reactions *via* enhanced CDT after intravenous injection.

indicates that they are promising biomedical carriers. These results indicate that this method can successfully synthesize evenly dispersed mFe_3O_4 nanoparticles.

To prepare M-mFeP@O_2-G nanoparticles, we extracted the membranes of K7M2 osteosarcoma cells and coated mFeP@O_2-G nanoparticles with these membranes. The successful fusion of osteosarcoma cell membranes with mFeP@O_2-G nanoparticles was further confirmed using TEM. First, the extracted osteosarcoma cell membranes were hollow vesicles, suggesting that their cavities can encapsulate the mFeP@O_2-G nanoparticles *via* an extrusion method using extruders of different sizes (Fig. 2A). At the same time, we compared the TEM images of the mFeP@O_2-G and M-mFeP@O_2-G nanoparticles (Fig. 2B and C), and a clear core–shell structure was present, indicating the presence of unilamellar cell membranes on the mFeP@O_2-G nanoparticles. Dynamic light scattering analysis also revealed that the hydrodynamic diameters of mFeP@O_2-G and M-mFeP@O_2-G nanoparticles were 128.0 ± 2.0 nm and 151.9 ± 3.3 nm, respectively (Fig. 2D). These results indicate that the extracted osteosarcoma cell membranes can be successfully coated on the surface of mFeP@O_2-G nanoparticles *via* extrusion. The zeta potential of mFeP@O_2-G nanoparticles was −7.51 ± 1.81 mV, which may be attributed to the residual carboxyl groups on the surface of the mFeP@O_2-G nanoparticle core after being ionized. After coating with cell membranes, the charge of the M-mFeP@O_2-G nanoparticles was further reduced to −15.26 ± 0.45 mV, which may be attributed to the surface charge of the cell membranes, suggesting the successful coating of cell membranes (Fig. 2E). In addition, the colloidal stability and dispersion performance of the M-mFeP@O_2-G nanoparticles were further examined by measuring their size and polydispersity coefficient (PDI) for a week. The M-mFeP@O_2-G nanoparticles showed a negligible size change and a low PDI in deionized water, PBS, and Dulbecco's modified Eagle's medium (DMEM) for one week, without any notable changes in particle size and PDI (Fig. 2F). Even after incubation in DMEM and PBS for one week, the size of the M-mFeP@O_2-G nanoparticles was still approximately 150 nm, with a narrow PDI. The appearance of the M-mFeP@O_2-G nanoparticles in different media was also recorded. No obvious precipitation was observed, and the M-mFeP@O_2-G nanoparticles still exhibited a good dispersion (Fig. S4A). Meanwhile, the M-mFeP@O_2-G nanoparticles still maintained good Dundar phenomena and strong magnetism (Fig. S4B), which was attributed to their uniform particle size distribution and negative charge, suggesting that M-mFeP@O_2-G nanoparticles could still be applied for further biomedical applications. In addition, we conducted precise elemental mapping of the mFeP@O_2-G nanoparticles using energy dispersive spectroscopy (EDS). We found that Fe, F, O, and N were clearly and uniformly distributed on the mFeP@O_2-G nanoparticles, which confirmed the successful loading of GOx and PFP (Fig. 2G). The hemocompatibility of the M-mFeP@O_2-G nanoparticles was also evaluated using red blood cells from rabbits. No hemolysis occurred upon treatment with mFeP@O_2-G or M-mFeP@O_2-G nanoparticles, which showed that these nanoparticles did not cause hemolysis and could be safely used for intravenous injection with good biocompatibility (Fig. S5).

Sodium dodecyl sulfate–polyacrylamide gel electrophoresis (SDS–PAGE) and western blotting were performed to further verify whether the tumor cell membrane surface proteins remained intact after coating the surface of the mFeP@O_2-G nanoparticles. As shown in Fig. 2H, the protein bands of M-mFeP@O_2-G nanoparticles were consistent with those of the K7M2 cell membranes. Similarly, several marker proteins on the surface of K7M2 osteosarcoma cells were detected, including CD47 [41], E-cadherin, galectin-3, and glycoprotein 100 (gp100) [42]. CD47, a "do not eat me" marker protein, plays a significant role in escaping phagocytosis by macrophages [43]. E-cadherin, galectin-3, and gp100 play significant roles in homologous targeting and are also marker proteins of tumor cells [44,45]. As shown in

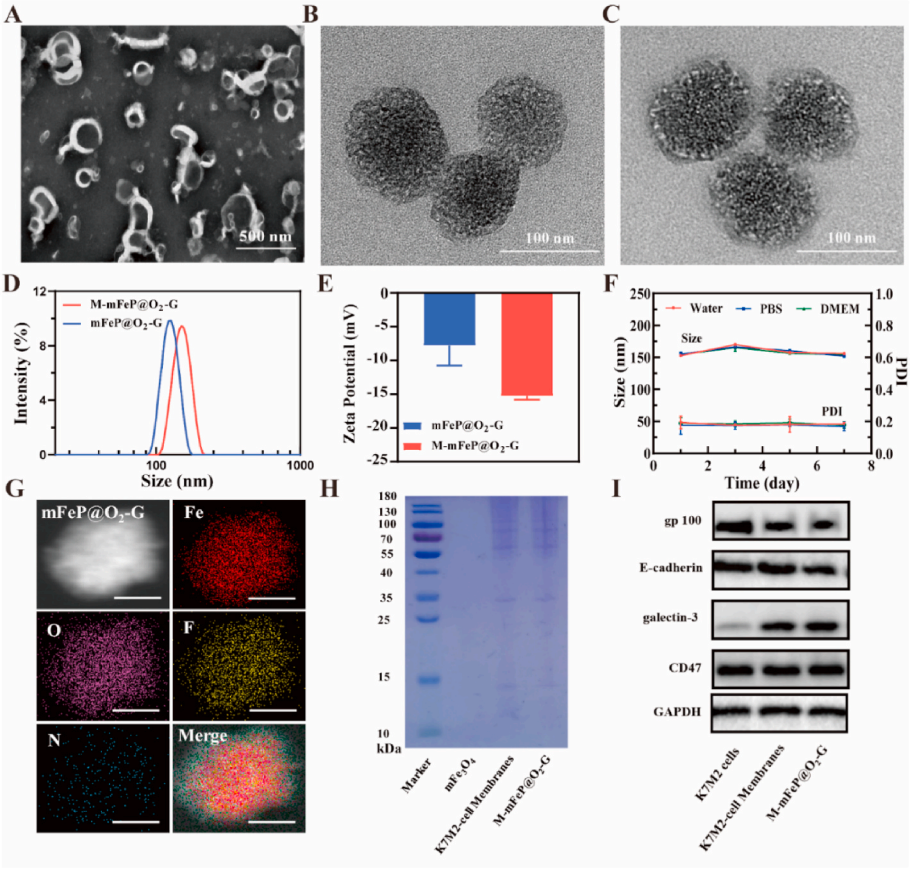

Fig. 2. Characterization of biomimetic M-mFeP@O_2-G nanoparticles. A) TEM images of membrane vesicles of K7M2 osteosarcoma cells. B) TEM images of mFeP@O_2-G nanoparticles. C) TEM images of M-mFeP@O_2-G nanoparticles. D, E) Size distribution and zeta potentials of mFeP@O_2-G and M-mFeP@O_2-G nanoparticles. F) Size distribution and PDI stability of M-mFeP@O_2-G nanoparticles. G) Elemental mapping of mFeP@O_2-G nanoparticles. Scale bar: 50 nm. H) SDS–PAGE analysis of mFe_3O_4 nanoparticles, K7M2-cell membranes, and M-mFeP@O_2-G nanoparticles. I) Western blotting analysis of K7M2 cells, K7M2-cell membranes, and M-mFeP@O_2-G nanoparticles.

Fig. 2I, these proteins were preserved on the surface of K7M2 cells, K7M2-cell membranes and M-mFeP@O_2-G nanoparticles, indicating the preparation of M-mFeP@O_2-G nanoparticles did not destroy the surface membrane proteins and retained the composition of the original membrane proteins of K7M2-cell membranes. Based on the above experiments, K7M2 cell membrane-coated nanoparticles were successfully prepared and provided the potential homologous targeting of the prepared nanoparticles.

2.2. Photothermal properties of M-mFeP@O_2-G nanoparticles in vitro

Ideally, photothermal materials should possess excellent photothermal conversion performance for biological PTT. Therefore, the *in vitro* photothermal performance of the M-mFeP@O_2-G nanoparticles was evaluated, as shown in Fig. 3. The temperature of the M-mFeP@O_2-G nanoparticles increased rapidly upon exposure to an 808 nm laser at different concentrations and laser power densities (Fig. 3A and B). These results showed that the photothermal performance of M-mFeP@O_2-G nanoparticles were both laser power density- and concentration-dependent. The M-mFeP@O_2-G nanoparticles can convert laser energy into heat, as shown in Fig. 3C. Moreover, the M-mFeP@O_2-G nanoparticles exhibited excellent photothermal stability without obvious temperature decay after five laser-on/off cycles, which allowed repeated PTT (Fig. 3D). In addition, the photothermal conversion efficiency (η) of M-mFeP@O_2-G nanoparticles was calculated according to a method reported in the literature, which is important for clinical applications [46]. The η of the M-mFeP@O_2-G nanoparticles was calculated to be 36.83% upon irradiation with an 808 nm laser (Fig. 3E). Taken together, the prepared M-mFeP@O_2-G nanoparticles showed high photothermal conversion efficiency and excellent photothermal stability, which is important for treating tumors using PTT.

After verifying the excellent photothermal performance of the M-mFeP@O_2-G nanoparticles, their Fe ion release rate was investigated *in vitro* at different pH values. As shown in Fig. 3F, the amount of Fe ions released from the M-mFeP@O_2-G nanoparticles increased slowly over time at pH 7.4, where only 1.46% of the Fe ions were released within 24 h. In contrast, the amount of Fe ions released increased considerably at pH 6.0, reaching 8.24% within 24 h. This result showed that M-mFeP@O_2-G nanoparticles were pH-sensitive, which was attributed to the fact that mFe_3O_4 nanoparticles decomposed more easily into free Fe ions at pH 6.0 than in a neutral medium. In addition, the coated cell membranes might have effectively avoided the burst release of Fe ions, thus preventing the large release of Fe ions in normal tissues and releasing them quickly in acidic tumor tissues. This result is further proof that this system adapts to the TME. In addition, the release of Fe ions was further enhanced under 808 nm laser irradiation. With this, more Fe ions could participate in the Fenton reaction to produce more ·OH to kill tumors, suggesting that PTT can further enhance CDT synergistically and kill tumor cells.

PFP, a type of perfluorocarbon compound, has a large O2 reservation capacity and has been used as an artificial blood and contrast agent in ultrasonography and magnetic resonance imaging [47,48]. The boiling

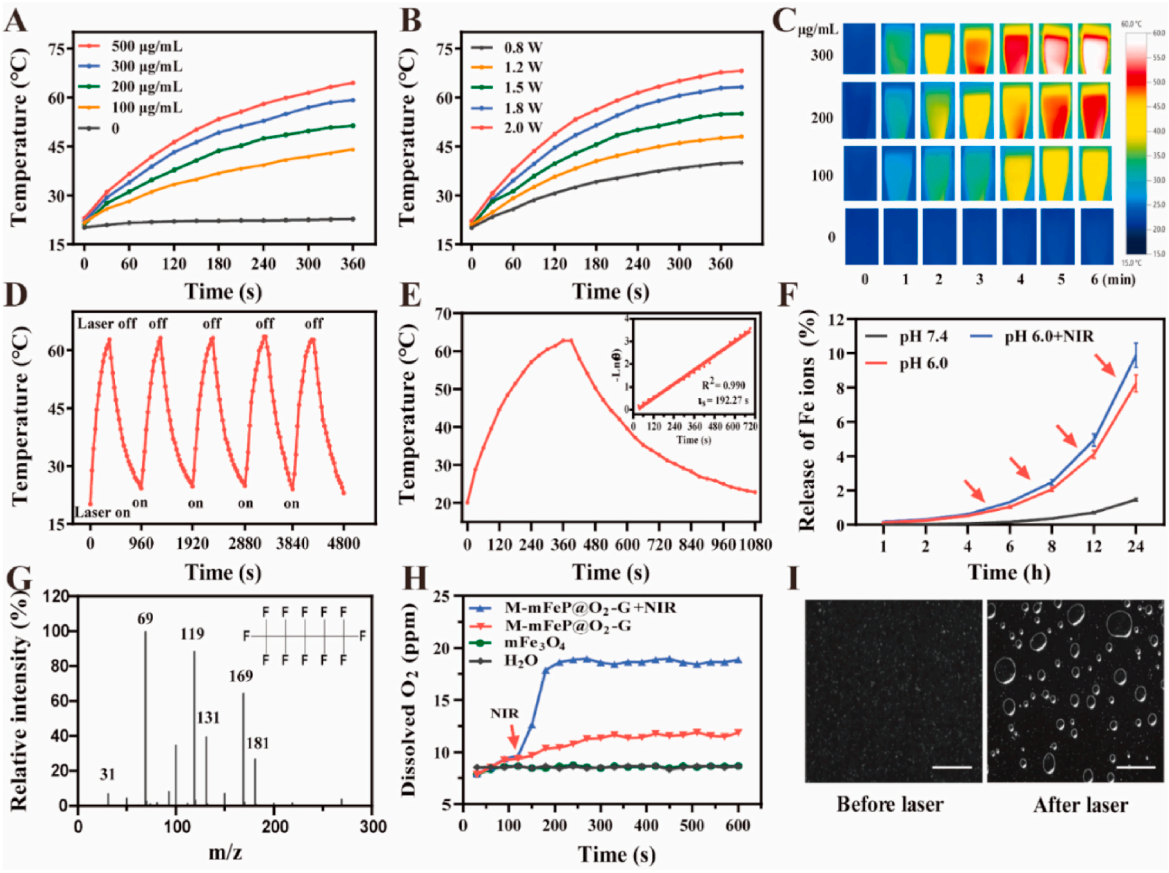

Fig. 3. Photothermal properties of M-mFeP@O_2-G nanoparticles *in vitro*. A) Temperature change curves of different concentrations of M-mFeP@O_2-G nanoparticles during NIR laser irradiation. B) Temperature change curves of M-mFeP@O_2-G nanoparticles during NIR laser irradiation at different powers. C) Thermographic images of M-mFeP@O_2-G nanoparticles during NIR laser irradiation. D) Photothermal curves of M-mFeP@O_2-G nanoparticles for five heating/cooling cycles. E) Photothermal performance of M-mFeP@O_2-G nanoparticles and the corresponding linear relationship between -Ln (θ) and time (s). F) *In vitro* Fe ion release behavior of M-mFeP@O_2-G nanoparticles at pH 7.4, pH 6.0, and pH 6.0 + NIR. G) GC–MS spectrum of M-mFeP@O_2-G nanoparticles. H) Time-dependent changes in dissolved oxygen concentrations in the M-mFeP@O_2-G solutions before and after laser irradiation. I) Photographs of bubble generation in the M-mFeP@O_2-G solution before and after laser irradiation. Scale bar: 200 μm.

point of PFP increases to 40–50 °C *in vivo* after intravenous injection, although its original boiling point is only 29 °C [49]. Therefore, an O_2-saturated PFP transformed into the body could release O2 with an increase in temperature due to the photothermal effect of the mFe_3O_4 nanoparticles under 808 nm laser radiation. First, the loading of PFP in the nanoparticles was confirmed *via* gas chromatography–mass spectrometry (GC–MS). The fragment ions (m z^{-1}) detected *via* mass spectrometry matched well with the corresponding standards (Fig. 3G and Fig. S6), indicating the successful loading of PFP. To visually monitor the oxygen-carrying and photothermal-responsive capacity of the M-mFeP@O_2-G nanoparticles adsorbed with PFP droplets, we used a portable dissolved oxygen meter to measure the oxygen concentration in different solutions. As shown in Fig. 3H, the dissolved oxygen concentration in the M-mFeP@O_2-G solution was significantly higher than that in water and the mFe_3O_4 solution, demonstrating the excellent oxygen-carrying capacity and gradual release profile of PFP. Notably, the oxygen concentration in the M-mFeP@O_2-G solution increased dramatically upon irradiation with an 808 nm laser, which demonstrates that the oxygen release from PFP is more sensitive under external NIR. Optical microscopy was also employed to capture images of M-mFeP@O_2-G solutions on glass slides before and after laser irradiation at a power intensity of 1.8 W cm^{-2} for 5 min. As shown in Fig. 3I, many microbubbles were observed after laser irradiation. These results indicate that the oxygen loaded in PFP can be fully released under photothermal stimulation, improving the O_2 concentration and alleviating the hypoxic state of the TME, and providing O2 for the cascade reactions to enhance antitumor CDT.

2.3. *In vitro* catalytic performance of M-mFeP@O_2-G nanoparticles

Glucose is an important source of energy and nutrients for the growth and proliferation of tumor cells [50]. GOx can catalyze glucose in the TME into gluconic acid and H_2O_2, thus effectively cutting off the supply of nutrients and energy to the tumor while blocking the growth of blood vessels, realizing tumor starvation treatment [51]. First, the loading capacity of GOx was calculated to be 5.03% *via* thermogravimetric analysis (Fig. S7), indicating the successful loading of GOx. Next, to assess whether the activity of GOx loaded in M-mFeP@O_2-G nanoparticles was degraded, we compared the activity of free GOx, M-mFeP@O_2-G nanoparticles, and M-mFeP@O_2-G nanoparticles upon laser radiation (808 nm, 1.8 w cm^{-2}, 10 min) using a CheKine™ Glucose Oxidase Activity Assay Kit. The results showed that there was no significant difference in the GOx enzyme activity between the free GOx, M-mFeP@O_2-G, and M-mFeP@O_2-G + NIR groups, indicating that the enzyme activity of GOx was not affected by the preparation process or laser irradiation (Fig. S8A). This may be attributed to the encapsulation of the nanoparticles with cell membrane materials, which shielded a large amount of GOx from direct contact with the external environment, thereby preventing enzyme degradation. Next, the GOx enzyme activity in M-mFeP@O_2-G nanoparticles was investigated at different pH values. The results showed that the enzyme activity at pH 6.0 was higher than that under neutral conditions, which was consistent with previous studies [52], indicating that M-mFeP@O_2-G nanoparticles were adaptive to the TME (Fig. S8B). In addition, the storage stability of GOx loaded in M-mFeP@O_2-G nanoparticles was also investigated. There was no significant degradation of the loaded nanoparticles, and GOx

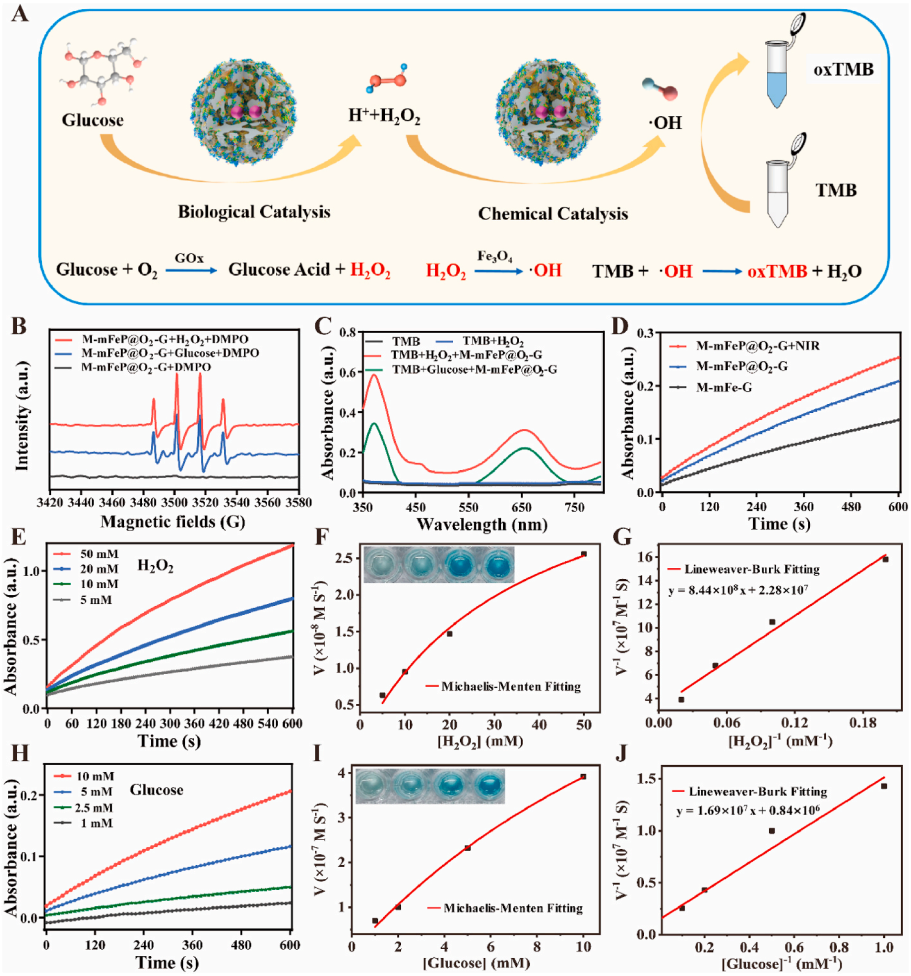

Fig. 4. *In vitro* characterization of the catalytic performance of M-mFeP@O_2-G nanoparticles. A) Schematic illustration of the reactions catalyzed by the M-mFeP@O_2-G nanoparticles. B) EPR spectrum of M-mFeP@O_2-G nanoparticles with the addition of glucose or H_2O_2 at pH 5.2 in the presence of DMPO. C) UV–vis absorption spectra of different TMB solutions at pH 5.2. D) Time-course absorbance of M-mFeG, M-mFeP@O_2-G and M-mFeP@O_2-G + NIR nanoparticles upon the addition of the same concentrations of β-D-glucose (10 mM). E, H) Time-course absorbance of M-mFeP@O_2-G nanoparticles upon the addition of various concentrations of H_2O_2 (5, 10, 20, and 50 mM) or β-D-glucose (1, 2.5, 5, and 10 mM). F, G, I, J) Michaelis–Menten kinetics and Lineweaver–Burk plots of the M-mFeP@O_2-G nanoparticles.

maintained >90% of its activity after one week of storage (Fig. S8C). Therefore, the activity of GOx can be maintained after stable storage for a week at 4 °C and is not affected by the preparation methods. Moreover, GOx has higher activity in the TME than in neutral conditions, which is adaptive to the TME.

As illustrated in Fig. 4A, in the mechanism of catalytic therapy, M-mFeP@O_2-G nanoparticles first reached the tumor site, and then the K7M2 cell membrane coating disintegrated to release Fe ions and GOx under the acidic conditions of the TME. The released Fe ions can then induce Fenton reactions by generating ·OH, and GOx can catalyze glucose into H_2O_2 and gluconic acid, which induces the self-amplifying catalytic cascade reactions *in situ*. Therefore, to investigate the generation of ·OH, 100 mM dimethyl pyridine N-oxide (DMPO) was applied to trap the short-lived ·OH to form relatively longer-living ·OH-DMPO adducts, which could be detected *via* electron paramagnetic resonance (EPR). As shown in Fig. 4B, considerable levels of ·OH were generated in the presence of H_2O_2, as demonstrated by the characteristic ·OH signals in the EPR spectrum. These results were caused by Fenton reactions between the Fe ions released from the mFe_3O_4 nanoparticles and H_2O_2 under mildly acidic conditions, resulting in a large amount of ·OH generated. Similarly, this reaction also generated a notable amount of ·OH in the presence of glucose. This was attributed to the released GOx that catalyzes the conversion of glucose into H_2O_2, and subsequently, the generated H_2O_2 can further react with the released Fe ions to generate ·OH. However, no signal was observed in the spectrum when neither H_2O_2 nor glucose was present in the system, indicating that no Fenton reaction occurred. All these results showed that Fe ions could produce Fenton reactions with endogenous H_2O_2 under the conditions of the TME and generate large amounts of ·OH to kill tumors. At the same time, encapsulated GOx can not only deplete glucose within tumor cells as starvation therapy but also generate large amounts of H_2O_2, which can further enhance the Fenton reaction to produce more ·OH.

The mFe_3O_4 nanoparticles showed catalase-like activity under neutral pH conditions and decomposed H_2O_2 into H_2O and O_2. In contrast, they exhibited peroxidase-like activity in an acidic environment and can disintegrate H_2O_2 into ·OH [53]. Therefore, a typical 3,3,5,5-tetramethylbenzidine (TMB) color reaction was performed to further evaluate the ·OH generation activity of M-mFeP@O_2-G nanoparticles. UV–vis absorption spectroscopy was used to monitor the production of the colorimetric product oxidized TMB (oxTMB), where a signal peak should be observed at 652 nm. As shown in Fig. 4C, no obvious signal peak was observed in the absence of TMB alone and TMB with H_2O_2, suggesting that no oxidation reaction occurred in either group. As expected, when M-mFeP@O_2-G nanoparticles, H_2O_2, and TMB are present, a characteristic peak at 652 nm can be clearly observed in the UV–Vis spectrum, confirming that the nanoparticles can undergo the Fenton reaction to generate toxic ·OH. Similarly, a characteristic peak at 652 nm was observed when M-mFeP@O_2-G nanoparticles, glucose, and TMB were present in the reaction system in the absence of H_2O_2. This result showed that the GOx loaded in the M-mFeP@O_2-G nanoparticles can also undergo a catalytic reaction under the action of glucose to generate H_2O_2, subsequently generating ·OH, which can induce the cascade reaction to kill tumors. Next, we monitored the ability of the M-mFeP@O_2-G nanoparticles to produce ·OH under different pH conditions (pH 7.4, 6.0, and 5.2). As shown in Fig. S9, the ability of the M-mFeP@O_2-G nanoparticles to generate ·OH was pH-dependent, wherein a decrease in pH gradually increased ·OH generation. This is mainly attributed to the accelerated release of Fe ions and the higher activity of GOx under acidic conditions, which is more adaptive to the TME and may be a promising antitumor treatment. To further verify the successful generation of the cascade, similarly, we also monitored the ability of different nanosystems (M-mFe-G, M-mFeP@O_2-G, M-mFeP@O_2-G + NIR) to produce ·OH under the same glucose concentration. As shown in Fig. 4D, the ability of the M-mFeP@O_2-G and M-mFeP@O_2-G + NIR nanoparticles to generate ·OH was stronger than that of M-mFe-G nanoparticles within a certain period of time. The results explained that the addition of oxygen and photothermal effects can both further enhance the activity of GOx, to produce more hydrogen peroxide and thus more ·OH, which can effectively kill tumor cells.

Next, typical Michaelis–Menten steady-state kinetics were used to investigate the catalytic ability of the M-mFeP@O_2-G nanoparticles. Initially, the catalytic activity of the M-mFeP@O_2-G nanoparticles was systematically explored using typical Michaelis–Menten steady-state kinetics with TMB and different concentrations of H_2O_2 (50, 20, 10, and 5 mM) as substrates (Fig. 4E–G). The time-course absorbance variation was acquired upon the addition of H_2O_2 into a solution of M-mFeP@O_2-G nanoparticles (100 μg mL^{-1}) in a 20 mM sodium acetate buffer (pH 5.2) (Fig. 4E). The corresponding concentration-changing rate (v_0) of cation-free radical production was calculated using the Beer–Lambert law according to Equation (1), which was fitted with the Michaelis–Menten curves (Equation (2), Fig. 4F). According to equation (3), to determine the Michaelis constant (K_M) and maximum reaction velocity (V_{max}) of the catalytic reaction M-mFeP@O_2-G nanoparticles, the Lineweaver–Burk plot was obtained, as shown in Fig. 4G. The K_M and V_{max} values were calculated to be 36.46 mM and 4.38 × 10^{-8} Ms^{-1} for M-mFeP@O_2-G nanoparticles, respectively, using different concentrations of H_2O_2 as the substrate. Hence, M-mFeP@O_2-G nanoparticles have good catalytic activity and can quickly catalyze H_2O_2 into toxic ·OH to kill tumors.

$$A = kbc \tag{1}$$

$$v_0 = \frac{Vmax \cdot [S]}{KM + [S]} \tag{2}$$

$$\frac{1}{v_0} = \frac{K_M}{V_{max}} \cdot \frac{1}{[S]} + \frac{1}{V\ max} \tag{3}$$

To assess if the GOx loaded in M-mFeP@O_2-G nanoparticles can catalyze the conversion of glucose in the TME into gluconic acid and H_2O_2, we measured the pH of the M-mFeP@O_2-G solution after adding different concentrations of β-D-glucose, as shown in Fig. S10. The experimental results show that the pH of the M-mFeP@O_2-G solution decreased with increasing β-D-glucose concentration, indicating that the GOx loaded in the mFe_3O_4 nanoparticles maintained its activity and can still catalyze the production of gluconic acid from glucose. Thus, M-mFeP@O_2-G nanoparticles can not only consume glucose from the TME and kill tumor cells *via* starvation therapy, but they can also catalyze the production of H_2O_2 and gluconic acid, which further promote the cascade reaction and enhance CDT. Similarly, the catalytic activity of M-mFeP@O_2-G nanoparticles was systematically explored using TMB and different concentrations of β-D-glucose (10, 5, 2.5, and 1 mM) as substrates (Fig. 4H–J). The time-course changes in absorbance were observed by adding β-D-glucose to a solution of M-mFeP@O_2-G nanoparticles (100 μg mL^{-1}) in sodium acetate buffer (Fig. 4H). The corresponding concentration-changing rate was calculated *via* the Beer–Lambert law and fitted with Michaelis–Menten curves (Fig. 4I). To determine the K_M and V_{max} of the catalytic reaction with M-mFeP@O_2-G nanoparticles, a Lineweaver–Burk plot was obtained, as shown in Fig. 4J. The K_M and V_{max} values were calculated to be 20.31 mM and 11.85 × 10^{-7} Ms^{-1} for the sequential M-mFeP@O_2-G nanoparticles, respectively. These results show that the M-mFeP@O_2-G nanoparticles have good catalytic activity in the presence of either glucose or H_2O_2, which guarantees that the M-mFeP@O_2-G nanoparticles could trigger a desirable and steady cascade catalytic reaction. Therefore, when the endogenous H_2O_2 in the TME is exhausted, GOx can catalyze glucose to generate large amounts of H_2O_2 *in situ* and facilitate the Fenton reaction to achieve antitumor effects.

2.4. *In vitro evaluation of targeting effect and immune escape performance*

To further verify the uptake and targeting ability of the M-

mFeP@O_2-G nanoparticles, DiD (red), a fluorescent probe, was loaded into mFe_3O_4 nanoparticles (defined as mFeD nanoparticles) which were then coated with K7M2-cell membranes (defined as M-mFeD), and labeled with DiO (green). Next, we incubated K7M2 cells with these dual-fluorophore-labeled nanoparticles for 6 h and observed them using a confocal laser scanning microscope. The results showed that around the blue DAPI-stained nuclei, the red signal from DiD (representing the mFe_3O_4 nanoparticle "core") and the green signal from DiO (representing the K7M2 cell membrane "shell") co-localized (Fig. 5A). These results indicated that the M-mFeP@O_2-G nanoparticles exhibited desirable cell uptake. Flow cytometry was then performed to assess the cell targeting and uptake of the M-mFeP@O_2-G nanoparticles *via* the mean fluorescence intensity of DiD in K7M2 cells. The uptake fluorescence intensity of M-mFeD was indicated by the apparent rightward shift of the curve compared with that of mFeD nanoparticles at both 2 h and 4 h of incubation (Fig. S11A). When the fluorescence intensity of mFeD nanoparticles at 2 h was defined as 100%, the fluorescence intensity of M-mFeD nanoparticles was 414.11% at 2 h, and that of the mFeD and M-mFeD nanoparticles were 460.12% and 658.74% at 4 h, respectively (Fig. S11B). These results indicate that nanoparticles coated with tumor cell membranes had improved cell uptake, which was associated with specific proteins on the K7M2 cell membranes. At the same time, the fluorescence imaging results also showed that the red fluorescence intensity was significantly increased after coating with the K7M2 cell

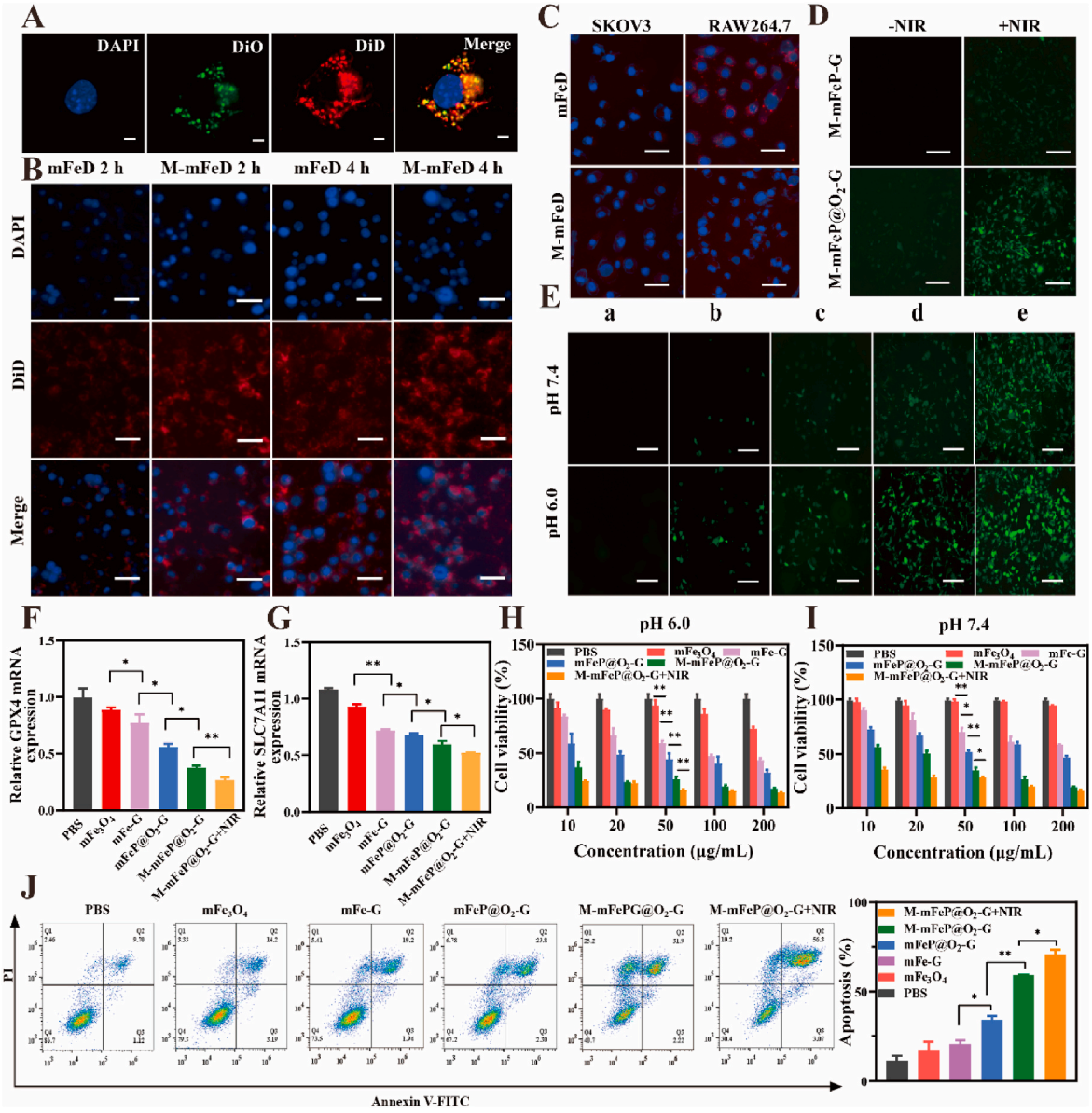

Fig. 5. *In vitro* cell targeting and antitumor activity of M-mFeP@O_2-G nanoparticles. A) Intracellular co-localization of the M-mFeD nanoparticle (shell: DiO/green; core: DiD/red). Scale bar: 5 μm. B) Intracellular uptake of mFeD and M-mFeD in SKOV3 and RAW 264.7 cells after 2 h and 4 h of incubation. Scale bar: 50 μm. The nuclei were stained with DAPI. C) Intracellular uptake of mFeD and M-mFeD in SKOV3 and RAW 264.7 cells after 4 h of incubation. Scale bar: 50 μm. The nuclei were stained with DAPI. D) Fluorescence images of K7M2 cells stained with DCFH-DA pre-incubated with M-mFeP-G (top) and M-mFeP@O_2-G (bottom) in a hypoxic environment. Scale bar: 50 μm. E) Fluorescence images of K7M2 cells after co-incubation with a) PBS, b) mFe_3O_4 nanoparticles, c) mFeP@O_2-G nanoparticles, d) M-mFeP@O_2-G nanoparticles, or e) M-mFeP@O_2-G nanoparticles + NIR under neutral (pH 7.4) and acidic (pH 6.0) conditions for 6 h and subsequent staining with DCFH-DA. Scale bar: 50 μm. F, G) Relative mRNA expression of GPX4 and SLC7A11 after different treatment. H, I) *In vitro* cell cytotoxicity of PBS, mFe_3O_4, mFe-G, mFeP@O_2-G, M-mFeP@O_2-G, and M-mFeP@O_2-G + NIR at different concentrations after incubation for 24 h at pH 6.0 and pH 7.4. Data are shown as mean ± SD, n = 4, ***P < 0.001, **P < 0.01, *P < 0.05. J) Flow cytometry analysis of K7M2 cells treated with PBS, mFe_3O_4, mFe-G, mFeP@O_2-G, M-mFeP@O_2-G, and M-mFeP@O_2-G + NIR for 24 h. The cells were stained with Annexin V-647 and PI for analysis.

membranes, which corresponded to the flow cytometry results (Fig. 5B).

We then selected SKOV3 ovarian tumor cells to further evaluate the homologous targeting capacity of the K7M2 osteosarcoma cell membrane-coated nanoparticles. There was no obvious difference in fluorescence intensity after incubating SKOV3 cells with M-mFeD and mFeD nanoparticles (Fig. 5C and Fig. S12A). However, higher fluorescence intensity was observed in the K7M2 cells treated with M-mFeD nanoparticles, indicating that the tumor cell membrane-coated nanoparticles possessed a stronger targeting ability to homologous tumor cells, which was due to the affinity between the surface membrane proteins present (Fig. 5B). Due to similar membrane proteins, nanoparticles modified with tumor cell membranes can have a significantly enhanced ability to target homotypic tumor cells, which ensures that the modified nanoparticles can better deliver cargo to the tumor site and reduce unnecessary toxicity and other side effects.

Nanoparticles coated with tumor cell membranes can usually escape phagocytosis by immune cells due to specific proteins on their surfaces [54,55]. Therefore, to verify that the K7M2 cell membrane-coated nanoparticles could escape macrophage phagocytosis, M-mFeD nanoparticles were incubated with RAW 264.7 cells. The red fluorescence signal intensity of the M-mFeD nanoparticle-treated group was lower than that of the mFeD nanoparticle-treated group (Fig. 5C and Fig. S12B). This is largely due to the presence of membrane proteins on the surface of K7M2 cells, especially CD47, which can induce phagocytosis escape. Therefore, when tumor cell membrane-coated nanoparticles enter the bloodstream, they can effectively avoid phagocytosis of immune cells, safely reaching the tumor sites to kill tumor cells.

2.5. *In vitro ROS and qPCR evaluation*

After confirming the cellular uptake and homologous targeting ability of the M-mFeP@O_2-G nanoparticles, their ·OH generation capacity was determined *via* the oxidation of DCFH-DA by ROS. As shown in Fig. S13A, the green fluorescence intensity of M-mFeP@O_2-G nanoparticles is indicated by the apparent rightward shift of the curve compared with that of the mFeP@O_2-G nanoparticles. Notably, the curve shifted the most to the right after the cells were treated with M-mFeP@O_2-G nanoparticles + NIR. These results showed that modification with cell membrane material could induce the nanoparticles to enter cells and produce more ·OH. Moreover, the additional photothermal effect could further enhance the Fenton reaction and produce more ·OH, killing tumors. When the fluorescence intensity of PBS is defined as 100%, the fluorescence intensities of the solutions containing mFeP@O_2-G and M-mFeP@O_2-G nanoparticles were 274.34% and 373.04%, respectively (Fig. S13B). Upon NIR treatment, the fluorescence intensity increased up to 563.91%, indicating that more ROS was produced. In addition, we also compared the generation of ROS at different pH values, and the fluorescence intensity at pH 6.0 was significantly higher than that at neutral pH (Fig. 5E). At the same time, the fluorescence imaging results also showed that the green fluorescence intensity was significantly increased after coating with the K7M2 cell membranes, and the strongest fluorescence intensity was achieved after 808 nm laser irradiation, similar to the flow cytometry results. These results indicate that the acidic environment of the TME was adaptive to the Fenton reaction and killed the tumor cells. This can be attributed to the fact that, under acidic conditions, more Fe ions are released, leading to the Fenton reaction, producing more ROS. At the same time, the GOx enzyme activity increased under acidic conditions. Hence, the results of the cellular uptake and homologous targeting assays suggest that nanoparticles coated with tumor cell membranes effectively entered tumor cells, synergized with photothermal agents *in vitro* to induce tumor cells to produce more ·OH, and promoted ferroptosis.

Ferroptosis is a programmed cell death caused by intracellular lipid peroxidation and plasma membrane rupture [20]. GPX4 is inactivated by GSH depletion and is a key regulator of ferroptosis and excessive accumulation of lipid peroxidation to lethal levels [21]. SLC7A11 mediates cystine uptake and glutamate release and is required for iron overload mediated iron death. Moreover, SLC7A11 is glucose dependent, and its expression level decreases with glucose consumption, thereby reducing antioxidant defense and promoting tumor cell death [56]. Therefore, we selected K7M2 tumor cells with high expression of GPX4 and SLC7A11, treated them with different nanosystems, and evaluated their mRNA expression levels in cells. The qPCR assays both showed the expression of mRNA level of GPX4 and SLC7A11 was obviously down-regulated when K7M2 cells were treated with different nanosystems compared with PBS, which was attribute to the presence of Fe ions in the nanosystems (Fig. 5F and G). While the cells treated with mFe-G and mFeP@O_2-G nanoparticles were more obviously compared with mFe_3O_4 nanoparticles alone. This may be attributed not only to the presence of Fe ions but also to the large amount of GOx and PFP loaded in the nanosystem, which could deplete glucose within tumor cells and produce H_2O_2 *in situ* for subsequent ·OH generation, and carry O_2 to enhance the cascade reaction, respectively. We can also see that mFeP@O_2-G nanoparticles coated with tumor cell membranes had further down-regulated the mRNA expression level, which was associated with specific proteins on the K7M2 cell membranes. In addition, external photothermal effect also made a certain contribution, which can promote the occurrence of ferroptosis. Taken together, these data demonstrated that the NIR-active mFeP@O_2-G nanoparticles could act as an efficient GPX4 and SLC7A11 inactivator, which may lead to collaborative apoptosis and ferroptosis of tumor.

Because of the porous structure and large surface area of mFe_3O_4 nanoparticles, mFe_3O_4 can function as a nanocarrier for PFP loading, which can absorb large amounts of O2 due to the van der Waals interactions between PFP and O_2 [57]. Therefore, to assess if the PFP-loaded O_2 has the ability to regulate hypoxic tumor environments, we first monitored the protein expression of hypoxia-inducible factor-1α (HIF-1α), which are major regulators of the intracellular hypoxia adaptation response, in K7M2 osteosarcoma cells [58]. Hypoxia can upregulate the expression of HIF-1α. As expected, the expression of HIF-1α protein was significantly downregulated in the presence of M-mFeP@O_2-G compared with that in the PBS and mFe_3O_4 alone-treated groups (Fig. S14A). The results showed that O_2-saturated PFP significantly improved intracellular O_2 levels and alleviated the hypoxic state of K7M2 osteosarcoma cells. More importantly, the expression of HIF-1α was further downregulated upon NIR laser irradiation. This result further proved that stimulating PFP to rapidly release oxygen bubbles under NIR is beneficial for relieving tumor hypoxia, which can achieve a strong synergistic antitumor effect. The gray ratio of HIF-1α to GAPDH was 34.5% in the M-mFeP@O_2-G group and 23.02% in M-mFeP@O_2-G + NIR groups, which were lower compared to the cells treated with PBS and mFe_3O_4 alone (67.5% and 66.5%, respectively) (Fig. S14B). Next, we further evaluated whether the O_2 loaded in PFP can play a therapeutic role in the hypoxic state of the TME. We simulated the state of tumor hypoxia and monitored ROS generation under hypoxic conditions. As shown in Fig. 5D, the green fluorescence intensity of the M-mFeP@O_2-G nanoparticles was significantly higher than that of the M-mFeP-G nanoparticles without O2 saturation upon irradiation with an 808 nm laser. When tumor cells are in a hypoxic condition, the O_2-loaded nanoparticles can release a large amount of O_2 under external photothermal stimulation, thus simultaneously relieving the tumor's hypoxic state and producing more ROS.

2.6. *In vitro cytotoxicity profiles*

These cell experiments demonstrated the good targeting ability and efficient production of ·OH induced by the nanoparticles fabricated in this study. To evaluate the killing ability of these nanoparticles on K7M2 osteosarcoma cells, their potential cytotoxicity and ability to induce apoptosis were evaluated. The *in vitro* cytotoxicity of the different nanoparticle formulations was evaluated *via* the CCK8 assay at various concentrations in both acidic (pH 6.0) and neutral (pH 7.4) culture

media for 24 h. The results showed that cell viability was highly dependent on the concentration of the nanoparticles and the pH of the media (Fig. 5H and I). The M-mFeP@O_2-G nanoparticle + NIR groups displayed remarkable inhibition of K7M2 cell growth, which had stronger inhibitory effects than mFe_3O_4, mFe-G, mFeP@O_2-G, or M-mFeP@O_2-G at pH 7.4. The cell growth inhibition rate at pH 6.0, which is higher than that in neutral culture media in all formations, also showed the best inhibition efficiency in the M-mFeP@O_2-G + NIR group, compared to that of the mFe_3O_4, mFe-G, mFeP@O_2-G, and M-mFeP@O_2-G groups. This could be attributed to the peroxidase-like activity of mFe3O4 nanoparticles in the acidic environment that can decompose H_2O_2 into ·OH and the increased enzymatic activity of GOx under acidic conditions. Additionally, the apoptosis of K7M2 cells was analyzed using Annexin-V647/PI double staining *via* flow cytometry. At a concentration of 50 μg mL^{-1}, the percentage of cell apoptosis induced by the M-mFeP@O_2-G nanoparticles + NIR was 70.83%, which was higher than that in the M-mFeP@O_2-G group (59.34%), the mFeP@O_2-G group (34.3%) and the mFe-G group (26.55%) (Fig. 5J). Collectively, these data suggest that the homologous targeting ability of the nanoparticles and their ability to generate ·OH from the cascade reaction contribute to their cytotoxicity and ability to induce apoptosis.

The efficacy of tumor cell membrane-coated nanoparticles for enhanced CDT cascade *in vitro* may indicate their potential *in vivo* therapeutic effects. To verify this, we examined the therapeutic properties of different nanoparticles in a subcutaneous tumor model in BALB/c mice bearing K7M2 osteosarcoma. The *in vivo* treatment cycles and administration methods were recorded as shown in Fig. 6A. First, to confirm the time when these nanoparticles aggregated at the tumor site and the targeting effect after the coating of cell membranes, we studied the *in vivo* fluorescence imaging of mice bearing one K7M2 osteosarcoma models at different time points. As shown in Fig. 6B, M-mFeD nanoparticles can efficiently aggregate with the tumor sites, and the fluorescence intensity was significantly stronger than that of the mFeD nanoparticles (Fig. S15). And the fluorescence intensity reached the

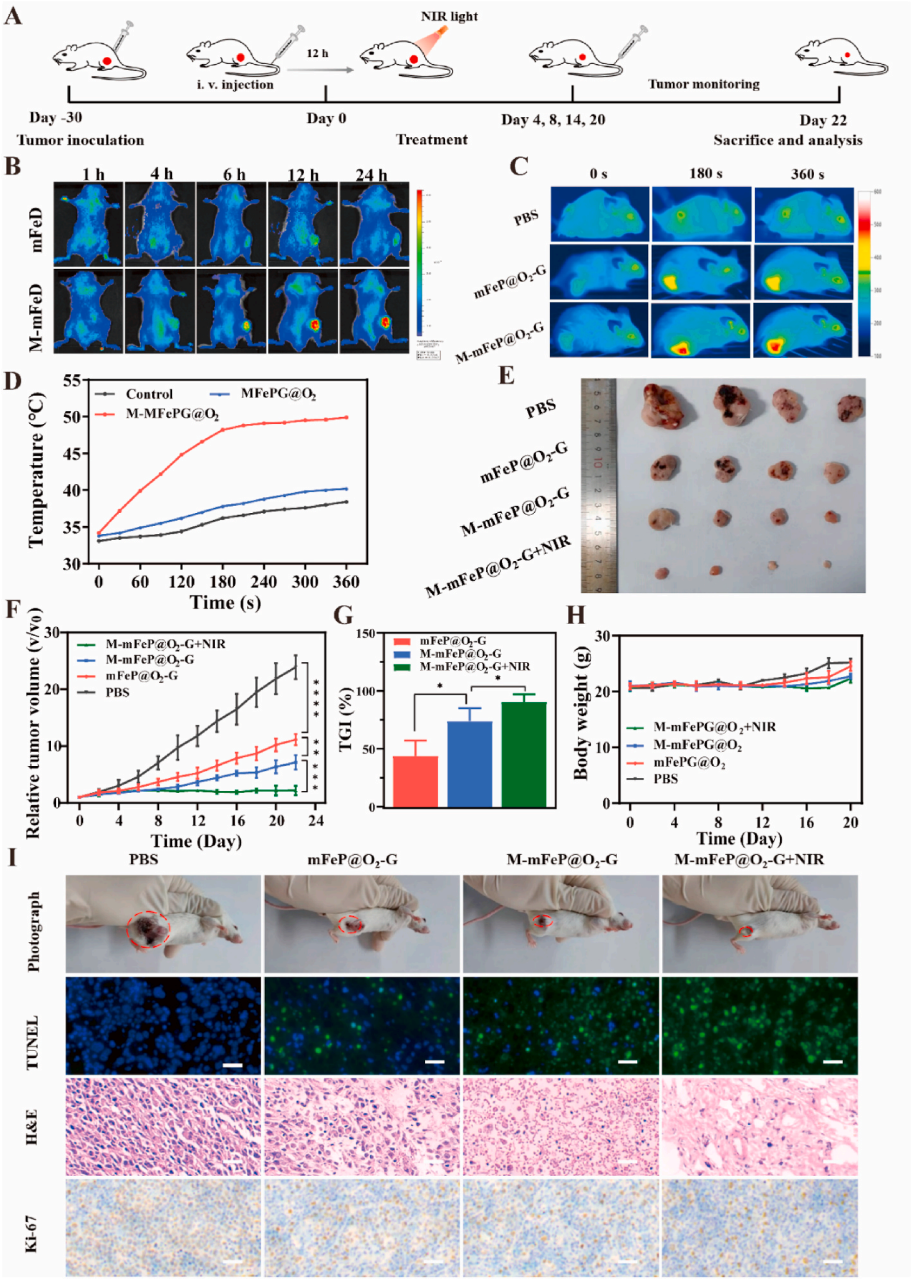

Fig. 6. *In vivo* evaluation of the tumor-suppressive effect of the fabricated nanoparticles. A) Experimental timeline for the antitumor efficacy study. B) *In vivo* fluorescence images at different time points post intravenous injection with M-mFeD and mFeD nanoparticles. C) Infrared thermographic maps of the irradiated areas 12 h after intravenous injection. D) Time-dependent temperature curves of the PBS, mFeP@O_2-G nanoparticles, and M-mFeP@O_2-G nanoparticles in the mouse subcutaneous ectopic tumor model upon irradiation with an 808 nm laser. E) Images of the tumor tissues collected from the test groups after 22 days of treatment. F) The average relative tumor volume *vs.* time curve after administration of the different nanoparticles to K7M2 osteosarcoma-bearing mice. G) TGI on day 22. H) Mouse body weight changes after different treatments. I) Images of the mice on day 22 and H&E, TUNEL, and Ki-67 staining of the tumor tissues after different treatments. Scale bar: 50 μm.

maximum value at 12 h, which could be used as the basis for subsequent photothermal irradiation. Then, to further evaluate whether the M-mFeP@O_2-G nanoparticles possess homologous targeting capacity owing to their membrane coating, the distribution of the M-mFeP@O_2-G nanoparticles in the BALB/c mice bearing K7M2 osteosarcoma tumors was investigated. Infrared thermographs (1.25 W cm^{-2}, 10 min) in the tumor locations were recorded, as shown in Fig. 6C. The temperature of the tumors in the mFeP@O_2-G nanoparticle group increased from 33.8 to 40.2 °C in 360 s, whereas those in the M-mFeP@O_2-G nanoparticle group showed a significant temperature increase from 34.2 °C to 48.2 °C in 180 s, reaching 49.9 °C in 360 s. This temperature remained unchanged under further irradiation, indicating that a stable heat exchange was achieved at this time point (Fig. 6D). This result indicated that coating the nanoparticles with K7M2 cell membranes could direct their accumulation at the tumor site. In addition, this result also shows that the NIR laser can penetrate the skin tissue and trigger the photothermal conversion of M-mFeP@O_2-G nanoparticles *in vivo*, inducing effective PTT.

2.7. In vivo evaluation of the tumor-suppressive effect

Encouraged by the *in vitro* results, we further evaluated the antitumor efficacy of the different nanoparticles *in vivo*. After treatment for 22 days, the tumors of BALB/c mice in all groups were dissected and weighed (Fig. 6E), and visually demonstrated that osteosarcoma cell growth could be effectively suppressed after the administration of mFeP@O_2-G, M-mFeP@O_2-G, and M-mFeP@O_2-G + NIR. After injection with PBS, no inhibitory effect on tumor growth was observed, and the relative average tumor volumes increased more rapidly compared with the other three groups (Fig. 6F). Within 22 days, the tumor growth rate in the mice administered with M-mFeP@O_2-G nanoparticles was remarkably lower than those treated with mFeP@O_2-G nanoparticles. Moreover, the tumor growth inhibition (TGI) rates of the M-mFeP@O_2-G and mFeP@O_2-G nanoparticles have been calculated to be 68.68% and 51.72%, respectively. Notably, M-mFeP@O_2-G nanoparticles irradiated with an 808 nm laser have the best tumor inhibition effect *in vivo*, with a TGI of 90.50% (Fig. 6G). Overall, the excellent therapeutic effects of M-mFeP@O_2-G nanoparticles + NIR laser irradiation could be attributed to the synergy of enhanced CDT, PPT, and starvation therapy, which showed clinical translation potential. This excellent antitumor effect of M-mFeP@O_2-G nanoparticles was mainly attributed to the homologous targeting of tumor cell membranes, which could direct the nanoparticles to the tumor site. At the same time, after these M-mFeP@O_2-G nanoparticles accumulated at the tumor sites, they could disintegrate to release Fe ions, GOx, and O_2 under the slightly acidic TME upon NIR laser irradiation. This can lead to a series of self-amplifying cascade catalytic reactions *in situ* and kill tumor cells *via* synergistic CDT and starvation therapy. The experimental results further suggest that PPT can enhance CDT to kill tumor cells, which not only promotes the release of Fe ions to drive the Fenton reaction and produce more ·OH, but also accelerates the catalytic ability of GOx to produce more H_2O_2, enhancing the Fenton reaction and killing even more tumor cells.

In addition, the body weights of the mice were recorded every two days. There were no significant changes in the body weights of the mice during the experimental period (Fig. 6H), suggesting that the M-mFeP@O_2-G nanoparticles had no obvious systematic toxicity and that the dose used was tolerable for the mice. At the same time, we also performed hematoxylin and eosin (H&E) staining to evaluate the histopathological changes in different organs (heart, liver, spleen, lungs, and kidneys) in the tumor model. The results showed no obvious organ toxicity after the administration of different nanoparticles compared with the PBS groups, indicating that the nanoparticles can be used for intravenous injection without toxicity to these organs (Fig. S16). This may be mainly attributed to the homologous targeting ability of tumor cell membranes, which could direct nanoparticles to reach tumor sites and not produce toxic side effects on normal tissues, resulting in a good therapeutic effect.

Additionally, H&E staining, terminal deoxynucleotidyl transferase-mediated dUTP nick-end labeling (TUNEL), and Ki-67 staining of tumor tissue slices were performed to evaluate the therapeutic outcome of these nanoparticles, the results of which were consistent with the results of tumor growth (Fig. 6I). H&E staining revealed that, compared with PBS treatment, the proportion of the dead zone in tumor sites increased when treated with different nanoparticles, especially upon irradiation with an 808 nm laser. The Ki-67 proliferation assay showed that the expression level of Ki-67 was significantly increased upon PBS treatment, whereas it was reduced in the mFeP@O_2-G, M-mFeP@O_2-G, and M-mFeP@O_2-G + NIR groups. The TUNEL assay also showed that the apoptosis of tumor cells increased when treated with different nanoparticles, especially when photothermal stimulation was applied. These results reveal the critical therapeutic outcomes of the different nanoparticles when used *in vivo* to treat tumors.

3. Conclusions

In summary, a TME-adaptive nanoplatform for synergistically enhancing CDT has been developed in this study and has achieved notable antitumor effects both *in vivo* and *in vitro*. We developed tumor cell membrane-functionalized nanoparticles by coating mFeP@O_2-G nanoparticles with K7M2 cell membranes for the targeted treatment of osteosarcoma. Owing to the specific marker proteins on the surface of the K7M2 cell membranes, M-mFeP@O_2-G nanoparticles showed effective immune escape and homologous targeting capacity to the tumor sites. Upon reaching the tumor site, the mFe_3O_4 $_n$anoparticles with excellent photothermal effects functioned as inducers of Fenton reaction, while the loaded GOx consumed glucose in the TME and catalyzed H_2O_2 decomposition, generating ·OH. Moreover, PFP provided O_2 for this cascade reaction, further enhancing the Fenton reactions. Thus, using the M-mFeP@O_2-G nanoparticles designed in this study is a promising strategy and a potential new platform for the precision treatment of osteosarcoma *via* synergistic CDT, starvation therapy, and PTT. We believe that this new enhanced CDT strategy using nanoparticles camouflaged with tumor cell membranes holds great promise for effectively treating tumors.

4. Materials and methods

4.1. Synthesis of mFe_3O_4 nanoparticles

Mesoporous Fe_3O_4 (mFe_3O_4) nanoparticles were synthesized according to a previously published method [59]. Briefly, $FeCl_3{\cdot}6H_2O$ (0.8 g), sodium citrate dehydrate (0.47 g), and sodium acetate (1.5 g) were dissolved in glycol (40 mL) under stirring to obtain a transparent solution, which was heated at 80 °C. The homogeneous solution was then transferred to a Teflon-lined stainless steel autoclave and heated to 200 °C. After an 8-h reaction period, the autoclave was cooled to room temperature and washed with water and ethanol. The final mFe_3O_4 nanoparticles were obtained *via* freeze-drying.

4.2. Synthesis of mFeP@O_2-G nanoparticles

To load PFP and GOx, the prepared mFe_3O_4 nanoparticles (10 mg) were transferred into a two-neck flask with a rubber stopper. Then, the air inside was evacuated for 10 min, followed by the injection of PFP (100 μL) into the flask. The system was ultrasonically oscillated for 5 min in an ice bath with 100 w power. The product was then dispersed in PBS containing GOx (10 mg) and stirred overnight in the dark. The final products were purified *via* centrifugation (10,000 rpm, 10 min) to remove excess PFP and GOx (mFeP-G). The precipitate was dispersed in PBS and stored in an oxygen chamber for 10 min to achieve oxygen saturation (mFeP@O_2-G).

4.3. Cell membrane isolation

K7M2-WT (K7M2) osteosarcoma cell membranes were obtained using a membrane protein extraction kit [60]. Briefly, the collected K7M2 cells (approximately 2–5 × 10^7 cells) were dispersed in the membrane protein extraction buffer solution and cooled in an ice bath for approximately 20 min. The cells were then transferred into a glass homogenizer and homogenized approximately 30–50 times. The resulting mixture was then centrifuged (2500 rpm, 10 min, 4 °C) to obtain the supernatant, which was centrifuged again (1500 rpm, 30 min, 4 °C) to collect the cell membranes. To obtain the membrane vesicles, the extracted membranes were ultrasonicated for 5 min in an ice bath with 100 w power and then extruded 20 times through 400-nm and 200-nm polycarbonate porous membranes using an Avestin mini extruder (ATS Engineering Canada). The harvested vesicles were stored at 4 °C until further use. A bicinchoninic acid (BCA) protein assay was used to analyze the total protein content in the obtained K7M2 cell membranes.

4.4. Synthesis of M-mFeP@O_2-G and M-mFeD nanoparticles

M-mFeP@O_2-G nanoparticles were fabricated by coating mFeP@O_2-G nanoparticles with the isolated K7M2 cell membranes [61]. Briefly, K7M2 cell membrane vesicles (1 mg mL^{-1}, 200 μL) and mFeP@O_2-G nanoparticles (1 mg mL^{-1}, 200 μL) were mixed and sonicated for 5 min in an ice bath and then extruded *via* a polycarbonate porous membrane (pore sizes of 400 nm and 200 nm) to harvest the M-mFeP@O_2-G nanoparticles. To prepare DiD dye-labeled nanoparticles, a 0.1 wt% DiD dye solution was first loaded into mFe_3O_4 nanoparticles (defined as mFeD nanoparticles) and then coated with the K7M2 cell membranes according to the former method, and the products were defined as M-mFeD nanoparticles.

4.5. Membrane protein characterization

SDS−PAGE was used to investigate the type and content of membrane proteins in mFe_3O_4 nanoparticles, K7M2 osteosarcoma cell membranes, and M-mFeP@O_2-G nanoparticles. RIPA lysis buffer was used to extract the total proteins from the cell membranes. The proteins were then analyzed *via* polyacrylamide gel electrophoresis and stained with Kaumas blue. Western blotting was used to identify the surface proteins present in the K7M2 osteosarcoma cell membranes. First, K7M2 osteosarcoma cells, K7M2 osteosarcoma cell membranes, and M-mFeP@O_2-G nanoparticles were lysed using RIPA buffer with 1 mM PMSF in an ice bath for 30 min and were quantified analysis using a BCA kit. These collected proteins were mixed with loading buffer, denatured by boiling in water for 5 min, and added to SDS-polyacrylamide gel in an electrophoresis chamber system (Bio-Rad Mini-Protean, USA). Next, the membranes were transferred onto polyvinylidene fluoride (PVDF) membranes and then blocked with 5% milk for approximately 1 h in an ice bath. The membranes were then probed with primary antibodies against CD47, glycoprotein 100, E-cadherin, and galectin-3 at 4 °C and then incubated with the corresponding secondary antibody [62,63]. Finally, the protein signals were visualized *via* a gel imaging system (Bio-Rad Gel Doc XR).

4.6. Hemolysis ratio calculation

Hemocompatibility was determined by evaluating the compatibility between red blood cells (RBCs) and nanoparticles [64]. First, the whole blood (2 mL) was injected into saline (5 mL) in a blood collection vessel. Subsequently, RBCs were obtained *via* centrifugation at 2000 rpm for 5 min three times. The purified RBCs were then divided into four tubes. Subsequently, 1 mL of saline (negative control), ultrapure water (positive control), and the mFeP@O_2-G and M-mFeP@O_2-G solutions were added to the tubes. All samples were then incubated at 37 °C for 3 h. Next, the samples were centrifuged at 2000 rpm for 5 min. Finally, the absorbance of the supernatant at 540 nm was measured using an ultraviolet spectrophotometer and the hemolysis rate was calculated using the following formula:

$$Hemolysis\ rate = \frac{A - B}{C - B} \times 100\% \tag{4}$$

where A is the absorbance of the nanoparticle solution, B is the absorbance of the negative control, and C is the absorbance of the positive control.

4.7. In vitro photothermal effect measurements

To investigate their NIR laser-induced photothermal conversion, different concentrations of M-mFeP@O_2-G nanoparticles (50, 100, 200, 300, 400, and 500 μg mL^{-1}, 0.4 mL) in Eppendorf tubes were exposed to an 808 nm laser with an output of 1.8 W cm^{-2} for 6 min. The real-time temperature was measured using an infrared thermal imager. Then, the M-mFeP@O_2-G nanoparticles (400 μg mL^{-1}) were irradiated with an 808 nm laser at powers of 0.5, 0.8, 1.2, 1.5, 1.8, and 2.0 W cm^{-2}, respectively. Finally, to study their photothermal stability, a M-mFeP@O_2-G solution (400 μg mL^{-1}) was irradiated in five cycles of 6 min irradiation on and 6 min off. The real-time temperatures of the solutions were recorded during irradiation.

In addition, the photothermal conversion efficiency (η) of the M-mFeP@O_2-G nanoparticles was determined according to a method established in previous studies [65]. Briefly, the M-mFeP@O_2-G solution (400 μg mL^{-1}, 0.4 mL) in vials was irradiated under an 808 nm NIR laser at an intensity of 1.8 W cm^{-2} for 450 s. Then, the laser was turned off, and the temperature changes of the solution were monitored with an IR camera. Finally, η was calculated using the following equation:

$$\eta = \frac{hA\Delta T_{max} - Q_s}{I\left(1 - 10^{-A_\lambda}\right)} \tag{5}$$

where η is the conversion efficiency value, ΔT_{max} is the maximum temperature change when the temperature reaches a steady-state under irradiation with an 808 nm NIR laser, I is the laser power density, and A_λ is the absorbance of the solution in the UV–vis spectrum. The values of Q_S and hA are unknown, but Q_S is related to the light absorbance of pure water and can be calculated using the following equation:

$$Q_s = \frac{m_w c_w \Delta T_{w-max}}{\Delta t} \tag{6}$$

where m_w is the mass of water, c_w is the heat capacity of water, $\Delta T_{w\text{-}max}$ is the maximum temperature change of water when the temperature reaches a steady state under irradiation with an 808 nm NIR laser, and Δt is the length of NIR laser irradiation treatment. The hA can then be calculated using the following equation:

$$\iota_s = \frac{m_D c_D}{hA} \tag{7}$$

where m_D is the mass of water used to suspend the nanoparticle, c_D is the heat capacity of water, and τ_s is the time constant, which can be calculated from the linear time-dependent data collected during the cooling period of the nanoparticle solutions.

In this study, we calculated the η value of the M-mFeP@O_2-G nanoparticles in detail. Here, Q_S was calculated to be 12.3 mW. The mass of water used to suspend the nanoparticles (m_D) was 0.4 g, the heat capacity of water (c_w) was 4.2 J g^{-1} K^{-1}, and the τ_s of M-mFeP@O_2-G nanoparticles was determined to be 192.31 s according to the linear time-dependent data collected during the cooling period as shown in Fig. 3D. Hence, according to equation (7), hA was calculated to be 8.74 × 10^{-3} W K^{-1}.

Finally, the maximum temperature change (ΔT_{max}) is 42.7 °C, and I is the laser power density which was 1.8 W cm^{-2}. The absorbance of 400

μg mL^{-1} M-mFeP@O_2-G nanoparticles at 808 nm in the UV–Vis spectrum (A_λ) was determined to be 0.291. According to Equation (5), the photothermal conversion efficiency (η) of M-mFeP@O_2-G nanoparticles was calculated to be 36.83%.

4.8. Selective and rapid release of Fe ions

M-mFeP@O_2-G solution (1 mg mL^{-1}, 1 mL) was sealed in a dialysis bag with a molecular weight cutoff of 7000 Da. The dialysis bags were then placed in PBS buffer solutions at different pH values (7.4 and 6.0), in the absence or presence of NIR laser irradiation at different time points (6 h, 8 h, 12 h and 24 h), and kept in a horizontal laboratory shaker at 37 °C. Under magnetic stirring, 1 mL of the sample solution was collected and replaced with an equal volume of fresh PBS at different time intervals. The concentration of the released Fe ions was measured using ICP–AES.

4.9. Measurement of O_2 release from M-mFeP@O_2-G triggered using NIR

To visually monitor the oxygen-carrying capacity of PFP, we used a portable dissolved oxygen meter to measure the oxygen concentration in deoxygenated water (prepared by boiling under a nitrogen atmosphere), mFe_3O_4, and M-mFeP@O_2-G nanoparticles [66,67]. Briefly, mFe_3O_4 and M-mFeP@O_2-G solutions (1 mg mL^{-1}, 1 mL) in an aqueous solution (50 mL) was pretreated with N_2 bubbles, and the oxygen concentration was recorded every 30 s for 10 min. In addition, the oxygen concentration of the M-mFeP@O_2-G solution in water was also recorded after irradiation with or without 808 nm NIR (1.8 W cm^{-2}, 8 min).

4.10. In vitro heat and NIR laser-induced bubble generation

Here, M-mFeP@O_2-G solution (1 mg mL^{-1}, 0.01 mL) was dropped onto a glass slide and covered with a coverslip. After irradiation with an 808 nm NIR laser at 1.8 W cm^{-2} for 5 min, the region of exposure was captured with an optical microscope.

4.11. Evaluation of GOx activity

GOx activity was measured using a CheKine™ Glucose Oxidase Activity Assay Kit, following the manufacturer's instructions. Briefly, M-mFeP@O_2-G nanoparticles (1 mg mL^{-1}, 0.01 mL) was added to 0.2 M glucose (50 μL) and then incubated at 37 °C for 20 min. Next, the chromogen (40 μL) was immediately added, and the solutions were incubated at 37 °C for 10 min. Finally, the absorbance of the solutions was measured at 580 nm. Therefore, according to the above method, we assessed the activity of the different nanoparticle preparations at different pH values. In addition, we evaluated the storage stability of the GOx enzyme for a week according to the above method.

4.12. In vitro free radical detection

The production of ·OH was detected using electron paramagnetic resonance (EPR) spectroscopy with DMPO as a spin trap to capture ·OH. Briefly, to detect the ·OH produced by Fe^{2+} and H_2O_2, M-mFeP@O_2-G nanoparticles (1 mg mL^{-1}, 150 μL) was mixed with a DMPO solution (50 mM) at pH 5.2 containing a glucose (50 mM) solution with or without H_2O_2 (50 mM). The solution was kept in a 37 °C water bath for 1 h, and the captured ·OH was detected using EPR spectroscopy.

4.13. Michaelis–Menten kinetics

A typical TMB color reaction was performed to systematically evaluate the ·OH generation activity of M-mFeP@O_2-G nanoparticles. UV–vis absorption spectroscopy was used to monitor the production of the colorimetric product oxidized TMB (oxTMB), and a signal peak appeared at 652 nm. Briefly, the TMB (1 mM, 1 mL) and M-mFeP@O_2-G nanoparticles (100 μg mL^{-1}) were added upon the addition of H_2O_2 (5 mM) or β-D-glucose (1 mM). NaAC buffer solution (20 mM, pH 5.2) was then added to a final volume (3 mL), and the absorbance change in the range of 350–800 nm was monitored after the reaction for 10 min. The same conditions were used to test the dependence of enzymatic activityon different pH values (pH 7.4, 6.0, and 5.2) by monitoring the absorbance change at 652 nm for 10 min. The same conditions were also used to test the dependence of enzymatic activityon different nanosystems (M-mFe-G, M-mFeP@O_2-G and M-mFeP@O_2-G + NIR) by monitoring the absorbance change at 652 nm for 10 min at the β-D-glucose concentration of 10 mM.

To determine the kinetic parameters of the reaction, the TMB (1 mM, 1 mL) was used to monitor the chromogenic reaction (λ = 652 nm) between M-mFeP@O_2-G nanoparticles upon the addition of varying H_2O_2 or β-D-glucose concentrations. An NaAC buffer solution (20 mM, pH 5.2) was added to a final reaction volume (3 mL). The Michaelis–Menten kinetic curves of the M-MFePG@O_2 nanoparticles were acquired by plotting the respective initial velocities against the concentrations of H_2O_2 and β-D-glucose. The Michaelis–Menten constant (KM) and maximal velocity (V_{max}) were calculated by creating Lineweaver–Burk plots.

4.14. Cell culture

K7M2 cells, the murine macrophage cell line RAW 264.7, and SKOV3 cells were obtained from the Shanghai Institute of Cells, Chinese Academy of Sciences, and were grown in high-glucose DMEM supplemented with 10% FBS and 1% streptomycin−penicillin at 37 °C in a humidified atmosphere with 5% CO_2.

4.15. Intracellular Co-localization

The fluorescent probe DiD was loaded into the mFe_3O_4 nanoparticles to investigate the location of the nanoparticles (M-mFeD), while the cell membranes were labeled with another fluorescent probe, DiO. K7M2 cells were seeded in 6-well plates. After culturing for 24 h, the medium was replaced with M-mFeD nanoparticles (1 mg mL^{-1}, 50 μL), and the cells were incubated for an additional 6 h. The cells were then washed three times with PBS and fixed with 4% paraformaldehyde solution at room temperature. Finally, the nuclei were stained with DAPI for fluorescent imaging and the cells were observed using a confocal laser scanning microscope (Rtec, UP-Sigma) with 405, 488, and 644 nm filters.

4.16. Evaluation of in vitro targeting capability

K7M2 cells were seeded in 6-well plates. After culturing for 24 h, the medium was replaced with mFeD nanoparticles (1 mg mL^{-1}, 50 μL) and M-mFeD nanoparticles (1 mg mL^{-1}, 50 μL) for 2 and 4 h, respectively. The cells were then washed three times with PBS and fixed with 4% paraformaldehyde solution at room temperature. Finally, the cell nuclei were stained with DAPI for fluorescence microscopy (IX71S1F-3, OLYMPUS, Japan). In addition, flow cytometry was used to quantify the fluorescence intensity. According to the same method above, the K7M2 cells were seeded in 6-well plates, and after the incubation with different nanoparticles, the cells were collected and analyzed using a CytoFLEX flow cytometer (Beckman Coulter, USA).

In addition, SKOV3 cells were seeded in 6-well plates. After culturing for 24 h, the medium was replaced with mFeD nanoparticles (1 mg mL^{-1}, 50 μL) and M-mFeD nanoparticles (1 mg mL^{-1}, 50 μL) for 4 h. Then, the cells were washed three times with PBS and fixed with 4% paraformaldehyde solution at room temperature. Finally, the nuclei were stained with DAPI and the cells were observed under fluorescence microscopy.

4.17. Evaluating escape from macrophage phagocytosis

RAW 264.7 cells were seeded in 6-well plates. After culturing for 24 h, the medium was replaced with mFeD nanoparticles (1 mg mL^{-1}, 50 μL) or M-mFeD nanoparticles (1 mg mL^{-1}, 50 μL), and the cells were incubated for another 4 h. Then, the cells were washed three times with PBS and fixed with 4% paraformaldehyde solution at room temperature. Finally, the nuclei were stained with DAPI and the cells were observed under fluorescence microscopy.

4.18. In vitro ROS generation assay

ROS generation *in vitro* was evaluated through the fluorescence change resulting from the ROS-induced oxidation of 2′-7′-dichlorodihydrofluorescein diacetate (DCFH-DA). Briefly, K7M2 cells were seeded in 6-well plates and incubated for 24 h. Then, the cells were treated with mFe_3O_4 nanoparticles, mFeP@O_2-G nanoparticles, M-mFeP@O_2-G nanoparticles, or M-mFeP@O_2-G nanoparticles + NIR (2 W cm^{-2}, 10 min). After another incubation for 6 h at different pH levels (6.0 and 7.4), the cells were washed with PBS and stained with DCFH-DA (10 μM) at 37 °C for 30 min and then observed *via* fluorescence microscopy. In addition, flow cytometry was performed to quantify the fluorescence intensity. According to the same method above, K7M2 cells were seeded in 6-well plates, and the cells were collected and analyzed *via* flow cytometry after incubation with the different nanoparticles.

Similarly, to assess whether PFP-loaded O_2 can regulate hypoxic tumor environments, K7M2 cells were seeded in 6-well plates in an anaerobic bag for 24 h. Then, the cells were treated with M-mFeP@O_2-G or M-mFeP-G nanoparticles for another 6 h before NIR irradiation (2 W cm^{-2}, 10 min). The cells were then washed with PBS, stained with DCFH-DA (10 μM) at 37 °C for 30 min, and observed under a fluorescence microscope.

4.19. Western blot analysis of HIF-1α expression

Western blotting was performed to evaluate changes in HIF-1α protein expression levels in K7M2 cells after treatment with the different nanoparticles. Briefly, K7M2 cells were seeded in 6-well plates. After 24 h of incubation, the cells were treated with PBS, mFeP@O_2-G, M-mFeP@O_2-G, or M-mFeP@O_2-G + NIR (2 W cm^{-2}, 10 min) for another 24 h. Then, the cells were collected and lysed using RIPA buffer with PMSF (1 mM) in an ice bath for 30 min, and the protein concentration of lysates were quantified for analysis *via* a BCA kit. According to the above method, the expression level of HIF-1α protein was detected *via* electrophoresis.

4.20. In vitro cytotoxicity assay

K7M2 cells were seeded in 96-well plates. After culturing for 24 h, the medium was replaced with DMEM diluted nanoparticles at different concentrations (10, 20, 50, 100, and 200 μg mL^{-1}) of mFe_3O_4 nanoparticles, mFe-G nanoparticles, mFeP@O_2-G nanoparticles, M-mFeP@O_2-G nanoparticles, or M-mFeP@O_2-G nanoparticles + NIR (2 W cm^{-2}, 10 min). After incubation for another 24 h at different pH levels (pH 6.0 and 7.4), CCK-8 (10 μL) solution was added to the cells. After incubation for 2 h, cell viability was evaluated by measuring the absorbance at 450 nm.

4.21. Apoptosis assays

K7M2 cells were seeded in 6-well plates. After culturing for 24 h, the medium was replaced with a concentration of 100 μg mL^{-1} of mFe_3O_4 nanoparticles, mFe-G nanoparticles, mFeP@O_2-G nanoparticles, M-mFeP@O_2-G nanoparticles, and M-mFeP@O_2-G nanoparticles + NIR (2 W cm^{-2}, 10 min). After incubation for 24 h, all cells were collected and stained with PI and Annexin V according to the Annexin V-FITC Apoptosis Detection Kitapoptosis detection kit and observed using a CytoFLEX flow cytometer.

4.22. Animal experiments

Female BALB/c mice (4–5 weeks old) were purchased from the Wuhan University Animal Biosafety Level III Lab. All animal handling protocols were approved by the Institutional Animal Care and Use Committee of the Animal Experiment Center of Sichuan University (arrpove number: 20211516A). K7M2 osteosarcoma models were established by subcutaneously injecting K7M2 cells (1×10^7 cells suspended in 100 μL PBS) into the right flank/leg of each mouse. Tumor size (V) was calculated as follows: V= (width^2 × length)/2 and measured every two days. After three weeks, the tumors, heart, liver, pleen, lungs and kidneys were collected from the sacrificed mice for further analysis.

4.23. In vivo fluorescence imaging

Firstly, mice bearing one K7M2 ostepsarcoma models were developed. Mice were intravenously injected with 100 μL of solutions containing mFeD and M-mFeD nanoparticles *via* tail vein at a concentration of 1 mg mL^{-1} per mouse. After different time points, mice were anesthetized and imaged *via* Maestro *in vivo* Imaging System (Caliper Life Sciences, IVIS Spectrum, USA). For ex vivo fluorescence imaging, mice were sacrificed at 24 h post-injection, and tumors and major organs (i.e., heart, liver, spleen, lung, and kidney) were dissected, washed with cold saline and then subjected to Maestro *in vivo* Imaging System to obtain the fluorescence images.

4.24. In vivo photothermal performance and tumor therapy

When the tumor volume grew to approximately 40 mm^3, the tumor-bearing mice were randomly divided into four groups (n = 4 each group) and administered with different treatments *via* tail vein injection: (1) PBS (control group), (2) mFeP@O_2-G nanoparticles, (3) M-mFeP@O_2-G nanoparticles, or (4) M-mFeP@O_2-G nanoparticles + NIR. NIR irradiation (808 nm) was performed for 10 min at a power intensity of 1.25 W cm^{-2} after intravenous injection for 12 h, and the *in vivo* images and temperatures were recorded using an infrared thermal imaging camera. The body weight and tumor volume of each mouse were recorded every two days. On the 22nd day, all the mice were sacrificed, and all the tumors and major organs, including the heart, liver, spleen, kidneys, and lungs, were harvested and preserved in 4% paraformaldehyde solution for H&E staining to evaluate the biosafety of the nanoparticles. The TUNEL assay and Ki-67 staining were also performed on the tumor tissues to evaluate the degree of tumor cell apoptosis.

4.25. Statistical analysis

All experimental data in this study was shown as mean ± standard deviation (SD). Statistical comparisons were calculated by using Student's t-test, and $p < 0.05$ was considered to be statistically significant.

Ethics approval and consent to participate

All procedures were conducted in accordance with the "Guiding Principles in the Care and Use of Animals" (China) and were approved by the Ethics Committee on Biomedical Research, West China Hospital of Sichuan University (**approve number: 20211516A**). Animal Ethics Committee have a meeting as scheduled, the participators have evaluated the care and use of animals described in the protocol of ***Tumor Microenvironment-Adaptive Nanoplatform Synergistically Enhances Cascaded Chemodynamic Therapy*** and find the procedures described as appropriate and acceptable.

CRediT authorship contribution statement

Yuemin Wang: Conceptualization, Investigation, Methodology, Writing – original draft. **Duan Wang:** Investigation. **Yuyue Zhang:** Investigation. **Hong Xu:** Investigation. **Luxuan Shen:** Investigation. **Jing Cheng:** Investigation. **Xinyuan Xu:** Investigation, Supervision. **Hong Tan:** Investigation, Supervision. **Xingyu Chen:** Conceptualization, Methodology, Supervision, Writing – review & editing, Data curation, Funding acquisition, Project administration. **Jianshu Li:** Conceptualization, Methodology, Supervision, Writing – review & editing, Data curation, Funding acquisition, Project administration.

Declaration of competing interest

The authors declare that they have no known competing financial interests or personal relationships that could have appeared to influence the work reported in this paper.

Acknowledgements

The authors thank the financial support from National Natural Science Foundation of China (51925304, 52173140 and 51803173), Sichuan Science and Technology Program (2021YJ0192) and the Opening Project of State Key Laboratory of Polymer Materials Engineering (Sichuan University) (Grant No. sklpme2020-4-13). All the animal procedures were performed under a protocol approved by the Laboratory Animal Center of the Animal Research Committee of Sichuan University.

Appendix A. Supplementary data

Supplementary data to this article can be found online at https://doi.org/10.1016/j.bioactmat.2022.09.025.

References

[1] K.D. Miller, R.L. Siegel, C.C. Lin, A.B. Mariotto, J.L. Kramer, J.H. Rowland, K. D. Stein, R. Alteri, A. Jemal, Cancer treatment and survivorship statistics, CA A Cancer J. Clin. 66 (2016) 271–289.
[2] D. Hanahan, Robert A. Weinberg, Hallmarks of cancer: the next generation, Cell 144 (2011) 646–674.
[3] A. Mangelinck, N. Habel, A. Mohr, N. Gaspar, B. Stefanovska, O. Fromigué, Synergistic anti-tumor effect of simvastatin combined to chemotherapy in osteosarcoma, Cancers 13 (2021).
[4] S. Hecker-Nolting, T. Langer, C. Blattmann, L. Kager, S.S. Bielack, Current insights into the management of late chemotherapy toxicities in pediatric osteosarcoma patients, Cancer Manag. Res. 13 (2021) 8989.
[5] X. Kong, R. Cheng, J. Wang, Y. Fang, K.C. Hwang, Nanomedicines inhibiting tumor metastasis and recurrence and their clinical applications, Nano Today 36 (2021), 101004.
[6] X. Wei, Y. Chen, X. Jiang, M. Peng, Y. Liu, Y. Mo, D. Ren, Y. Hua, B. Yu, Y. Zhou, Q. Liao, H. Wang, B. Xiang, M. Zhou, X. Li, G. Li, Y. Li, W. Xiong, Z. Zeng, Mechanisms of vasculogenic mimicry in hypoxic tumor microenvironments, Mol. Cancer 20 (2021) 7.
[7] R. Strack, Revealing the secretome, Nat. Methods 18 (2021), 1273-1273.
[8] W. Zhen, S. An, S. Wang, W. Hu, Y. Li, X. Jiang, J. Li, Precise subcellular organelle targeting for boosting endogenous-stimuli-mediated tumor therapy, Adv. Mater. 33 (2021), e2101572.
[9] X. Zhang, Z. Xi, J.O.a. Machuki, J. Luo, D. Yang, J. Li, W. Cai, Y. Yang, L. Zhang, J. Tian, K. Guo, Y. Yu, F. Gao, Gold cube-in-cube based oxygen nanogenerator: a theranostic nanoplatform for modulating tumor microenvironment for precise chemo-phototherapy and multimodal imaging, ACS Nano 13 (2019) 5306–5325.
[10] Y. Huang, S. Wu, L. Zhang, Q. Deng, J. Ren, X. Qu, A metabolic multistage glutathione depletion used for tumor-specific chemodynamic therapy, ACS Nano 16 (2022) 4228–4238.
[11] R. Zhang, L. Feng, Z. Dong, L. Wang, C. Liang, J. Chen, Q. Ma, R. Zhang, Q. Chen, Y. Wang, Z. Liu, Glucose & oxygen exhausting liposomes for combined cancer starvation and hypoxia-activated therapy, Biomaterials 162 (2018) 123–131.
[12] Z. Yu, Y. Hu, Y. Sun, T. Sun, Chemodynamic therapy combined with multifunctional nanomaterials and their applications in tumor treatment, Chem 27 (2021) 13953–13960.
[13] Y. Wang, T. Sun, C. Jiang, Nanodrug delivery systems for ferroptosis-based cancer therapy, J.Controlled Release 344 (2022) 289–301.
[14] S. Guan, X. Liu, C. Li, X. Wang, D. Cao, J. Wang, L. Lin, J. Lu, G. Deng, J. Hu, Intracellular mutual amplification of oxidative stress and inhibition multidrug resistance for enhanced sonodynamic/chemodynamic/chemo therapy, Small 18 (2022), e2107160.
[15] Z. Tang, Y. Liu, M. He, W. Bu, Chemodynamic therapy: tumour microenvironment-mediated Fenton and fenton-like reactions, Angew. Chem., Int. Ed. 58 (2019) 946–956.
[16] L.-S. Lin, J. Song, L. Song, K. Ke, Y. Liu, Z. Zhou, Z. Shen, J. Li, Z. Yang, W. Tang, G. Niu, H.-H. Yang, X. Chen, Simultaneous fenton-like ion delivery and glutathione depletion by MnO_2-based nanoagent to enhance chemodynamic therapy, Angew. Chem., Int. Ed. 57 (2018) 4902–4906.
[17] L. Zhang, S.-S. Wan, C.-X. Li, L. Xu, H. Cheng, X.-Z. Zhang, An adenosine triphosphate-responsive autocatalytic Fenton nanoparticle for tumor ablation with self-supplied H_2O_2 and acceleration of Fe(III)/Fe(II) conversion, Nano Lett. 18 (2018) 7609–7618.
[18] M. Huo, L. Wang, Y. Wang, Y. Chen, J. Shi, Nanocatalytic tumor therapy by single-atom catalysts, ACS Nano 13 (2019) 2643–2653.
[19] W. Feng, X. Han, R. Wang, X. Gao, P. Hu, W. Yue, Y. Chen, J. Shi, Nanocatalysts-augmented and photothermal-enhanced tumor-specific sequential nanocatalytic therapy in both NIR-I and NIR-II biowindows, Adv. Mater. 31 (2019), e1805919.
[20] S. Zhang, L. Jin, J. Liu, Y. Liu, T. Zhang, Y. Zhao, N. Yin, R. Niu, X. Li, D. Xue, S. Song, Y. Wang, H. Zhang, Boosting chemodynamic therapy by the synergistic effect of Co-catalyze and photothermal effect triggered by the second near-infrared light, Nano Lett. 12 (2020) 180.
[21] T. Liu, W. Liu, M. Zhang, W. Yu, F. Gao, C. Li, S.-B. Wang, J. Feng, X.-Z. Zhang, Ferrous-supply-regeneration nanoengineering for cancer-cell-specific ferroptosis in combination with imaging-guided photodynamic therapy, ACS Nano 12 (2018) 12181–12192.
[22] M. López-Lázaro, Dual role of hydrogen peroxide in cancer: possible relevance to cancer chemoprevention and therapy, Cancer Lett. 252 (2007) 1–8.
[23] S. Gao, H. Lin, H. Zhang, H. Yao, Y. Chen, J. Shi, Nanocatalytic tumor therapy by biomimetic dual inorganic nanozyme-catalyzed cascade reaction, Adv. Sci. 6 (2019), 1801733.
[24] M. Huo, L. Wang, Y. Chen, J. Shi, Tumor-selective catalytic nanomedicine by nanocatalyst delivery, Nat. Commun. 8 (2017) 357.
[25] C. Yang, M.R. Younis, J. Zhang, J. Qu, J. Lin, P. Huang, Programmable NIR-II photothermal-enhanced starvation-primed chemodynamic therapy using glucose oxidase-functionalized ancient pigment nanosheets, Small 16 (2020), 2001518.
[26] W.-P. Li, C.-H. Su, Y.-C. Chang, Y.-J. Lin, C.-S. Yeh, Ultrasound-induced reactive oxygen species mediated therapy and imaging using a Fenton reaction activable polymersome, ACS Nano 10 (2016) 2017–2027.
[27] F. Khadivi Derakshan, F. Darvishi, M. Dezfulian, C. Madzak, Expression and characterization of glucose oxidase from Aspergillus Niger in yarrowia lipolytica, Mol. Biotechnol. 59 (2017) 307–314.
[28] Z. Yu, P. Zhou, W. Pan, N. Li, B. Tang, A biomimetic nanoreactor for synergistic chemiexcited photodynamic therapy and starvation therapy against tumor metastasis, Nat. Commun. 9 (2018) 5044.
[29] Y. Wang, K. Zhang, X. Qin, T. Li, J. Qiu, T. Yin, J. Huang, S. McGinty, G. Pontrelli, J. Ren, Q. Wang, W. Wu, G. Wang, Biomimetic nanotherapies: red blood cell based core-shell structured nanocomplexes for atherosclerosis management, Adv. Sci. 6 (2019), 1900172.
[30] Z. Dong, X. Ke, S. Tang, S. Wu, W. Wu, X. Chen, J. Yang, J. Xie, J. Luo, J. Li, A stable cell membrane-based coating with antibiofouling and macrophage immunoregulatory properties for implants at the macroscopic level, Chem. Mater. 33 (2021) 7994–8006.
[31] L. Zhang, Y. Zhang, Y. Xue, Y. Wu, Q. Wang, L. Xue, Z. Su, C. Zhang, Transforming weakness into strength: photothermal-therapy-induced inflammation enhanced cytopharmaceutical chemotherapy as a combination anticancer treatment, Adv. Mater. 31 (2019), e1805936.
[32] C. Yao, W. Wu, H. Tang, X. Jia, J. Tang, X. Ruan, F. Li, D.T. Leong, D. Luo, D. Yang, Self-assembly of stem cell membrane-camouflaged nanocomplex for MicroRNA-mediated repair of myocardial infarction injury, Biomaterials 257 (2020), 120256.
[33] Y. Duan, M. Wu, D. Hu, Y. Pan, F. Hu, X. Liu, N. Thakor, W.H. Ng, X. Liu, Z. Sheng, H. Zheng, B. Liu, Biomimetic nanocomposites cloaked with bioorthogonally labeled glioblastoma cell membrane for targeted multimodal imaging of brain tumors, Adv. Funct. Mater. 30 (2020), 2004346.
[34] Wang, Y.; Xu, X.; Chen, X.; Li, J. Multifunctional biomedical materials derived from biological membranes. Adv. Mater. 2021, e2107406.
[35] M. Gao, C. Liang, X. Song, Q. Chen, Q. Jin, C. Wang, Z. Liu, Erythrocyte-membrane-enveloped perfluorocarbon as nanoscale Artificial red blood cells to relieve tumor hypoxia and enhance cancer radiotherapy, Adv. Mater. 29 (2017), 1701429.
[36] H. Sun, J. Su, Q. Meng, Q. Yin, L. Chen, W. Gu, P. Zhang, Z. Zhang, H. Yu, S. Wang, Y. Li, Cancer-cell-biomimetic nanoparticles for targeted therapy of homotypic tumors, Adv. Mater. 28 (2016) 9581–9588.
[37] J.-Y. Zhu, D.-W. Zheng, M.-K. Zhang, W.-Y. Yu, W.-X. Qiu, J.-J. Hu, J. Feng, X.-Z. Zhang, Preferential cancer cell self-recognition and tumor self-targeting by coating nanoparticles with homotypic cancer cell membranes, Nano Lett. 16 (2016) 5895–5901.
[38] C. Wang, B. Wu, Y. Wu, X. Song, S. Zhang, Z. Liu, Camouflaging nanoparticles with brain metastatic tumor cell membranes: a new strategy to traverse blood-brain barrier for imaging and therapy of brain tumors, Adv. Funct. Mater. 30 (2020), 1909369.
[39] R.H. Fang, A.V. Kroll, W. Gao, L. Zhang, Cell membrane coating nanotechnology, Adv. Mater. 30 (23) (2018), e1706759.
[40] Y.-J. Cheng, J.-J. Hu, S.-Y. Qin, A.-Q. Zhang, X.-Z. Zhang, Recent advances in functional mesoporous silica-based nanoplatforms for combinational photo-chemotherapy of cancer, Biomaterials 232 (2020), 119738.

[41] R. Majeti, M.P. Chao, A.A. Alizadeh, W.W. Pang, S. Jaiswal, K.D. Gibbs, N. van Rooijen, I.L. Weissman, CD47 is an adverse prognostic factor and therapeutic antibody target on human acute myeloid leukemia stem cells, Cell 138 (2009) 286–299.
[42] J.-W. Yoo, D.J. Irvine, D.E. Discher, S. Mitragotri, Bio-inspired, bioengineered and biomimetic drug delivery carriers, Nat. Rev. Drug Discov. 10 (2011) 521–535.
[43] W. Xie, W.-W. Deng, M. Zan, L. Rao, G.-T. Yu, D.-M. Zhu, W.-T. Wu, B. Chen, L.-W. Ji, L. Chen, K. Liu, S.-S. Guo, H.-M. Huang, W.-F. Zhang, X. Zhao, Y. Yuan, W. Dong, Z.-J. Sun, W. Liu, Cancer cell membrane camouflaged nanoparticles to realize starvation therapy together with checkpoint blockades for enhancing cancer therapy, ACS Nano 13 (2019) 2849–2857.
[44] A.V. Kroll, R.H. Fang, Y. Jiang, J. Zhou, X. Wei, C.L. Yu, J. Gao, B.T. Luk, D. Dehaini, W. Gao, L. Zhang, Nanoparticulate delivery of cancer cell membrane elicits multiantigenic antitumor immunity, Adv. Mater. 29 (2017), 1703969.
[45] B. Qiao, Y. Luo, H.-B. Cheng, J. Ren, J. Cao, C. Yang, B. Liang, A. Yang, X. Yuan, J. Li, L. Deng, P. Li, H.-T. Ran, L. Hao, Z. Zhou, M. Li, Y. Zhang, P.S. Timashev, X.-J. Liang, Z. Wang, Artificial nanotargeted cells with stable photothermal performance for multimodal imaging-guided tumor-specific therapy, ACS Nano 14 (2020) 12652–12667.
[46] T. Liu, M. Zhang, W. Liu, X. Zeng, X. Song, X. Yang, X. Zhang, J. Feng, Metal ion/tannic acid assembly as a versatile photothermal platform in engineering multimodal nanotheranostics for advanced applications, ACS Nano 12 (2018) 3917–3927.
[47] X. Wang, Y. Mao, C. Sun, Q. Zhao, Y. Gao, S. Wang, A versatile gas-generator promoting drug release and oxygen replenishment for amplifying photodynamic-chemotherapy synergetic anti-tumor effects, Biomaterials 276 (2021), 120985.
[48] C. Li, Y. Zhang, Z. Li, E. Mei, J. Lin, F. Li, C. Chen, X. Qing, L. Hou, L. Xiong, H. Hao, Y. Yang, P. Huang, Light-responsive biodegradable nanorattles for cancer theranostics, Adv. Mater. 30 (2018), 1706150.
[49] J. Zhang, H. Huang, L. Xue, L. Zhong, W. Ge, X. Song, Y. Zhao, W. Wang, X. Dong, On-demand drug release nanoplatform based on fluorinated aza-BODIPY for imaging-guided chemo-phototherapy, Biomaterials 256 (2020), 120211.
[50] H. Zhu, Y. Li, Z. Ming, W. Liu, Glucose oxidase-mediated tumor starvation therapy combined with photothermal therapy for colon cancer, Biomater. Sci. 9 (2021) 5577–5587.
[51] S. Song, J. Peng, Y. Wu, C. Li, D. Shen, G. Yang, J. Liu, P. Gong, Z. Liu, Biomimetic synthesis of A novel O_2-regeneration nanosystem for enhanced starvation/chemo-therapy, Nanotechnology 33 (2021), 025102.
[52] C.M. Wong, K.H. Wong, X.D. Chen, Glucose oxidase: natural occurrence, function, properties and industrial applications, Appl. Microbiol. Biotechnol. 78 (2008) 927–938.
[53] Y. Li, D. Wang, J. Wen, P. Yu, J. Liu, J. Li, H. Chu, Chemically grafted nanozyme composite cryogels to enhance antibacterial and biocompatible performance for bioliquid regulation and adaptive bacteria trapping, ACS Nano 15 (2021) 19672–19683.
[54] Y. Qu, B. Chu, X. Wei, Y. Chen, Y. Yang, D. Hu, J. Huang, F. Wang, M. Chen, Y. Zheng, Z. Qian, Cancer-cell-biomimetic nanoparticles for targeted therapy of multiple myeloma based on bone marrow homing, Adv. Mater. (2021), e2107883.
[55] C. Chu, L. Liu, S. Rung, Y. Wang, Y. Ma, C. Hu, X. Zhao, Y. Man, Y. Qu, Modulation of foreign body reaction and macrophage phenotypes concerning microenvironment, J. Biomed. Mater. Res., Part A 108 (1) (2020) 127–135.
[56] P. Koppula, L. Zhuang, B. Gan, Cystine transporter SLC7A11/xCT in cancer: ferroptosis, nutrient dependency, and cancer therapy, Protein Cell 12 (8) (2021) 599–620.
[57] F. Zhang, J. Zhuang, B. Esteban Fernández de Ávila, S. Tang, Q. Zhang, R.H. Fang, L. Zhang, J. Wang, A nanomotor-based active delivery system for intracellular oxygen transport, ACS Nano 13 (2019) 11996–12005.
[58] F. Zheng, J. Chen, X. Zhang, Z. Wang, J. Chen, X. Lin, H. Huang, W. Fu, J. Liang, W. Wu, B. Li, H. Yao, H. Hu, E. Song, The HIF-1α antisense long non-coding RNA drives a positive feedback loop of HIF-1α mediated transactivation and glycolysis, Nat. Commun. 12 (2021) 1341.
[59] S. Xuan, F. Wang, J.M.Y. Lai, K.W.Y. Sham, Y.-X.J. Wang, S.-F. Lee, J.C. Yu, C.H. K. Cheng, K.C.-F. Leung, Synthesis of biocompatible, mesoporous Fe_3O_4 nano/microspheres with large surface area for magnetic resonance imaging and therapeutic applications, ACS Appl. Mater. Interfaces 3 (2011) 237–244.
[60] S.-Y. Li, H. Cheng, B.-R. Xie, W.-X. Qiu, J.-Y. Zeng, C.-X. Li, S.-S. Wan, L. Zhang, W.-L. Liu, X.-Z. Zhang, Cancer cell membrane camouflaged cascade bioreactor for cancer targeted starvation and photodynamic therapy, ACS Nano 11 (2017) 7006–7018.
[61] Y. Wang, K. Zhang, T. Li, A. Maruf, X. Qin, L. Luo, Y. Zhong, J. Qiu, S. McGinty, G. Pontrelli, X. Liao, W. Wu, G. Wang, Macrophage membrane functionalized biomimetic nanoparticles for targeted anti-atherosclerosis applications, Theranostics 11 (2021) 164.
[62] Y. Qu, B. Chu, X. Wei, Y. Chen, Y. Yang, D. Hu, J. Huang, F. Wang, M. Chen, Y. Zheng, Z. Qian, Cancer-cell-biomimetic nanoparticles for targeted therapy of multiple myeloma based on bone marrow homing, Adv. Mater. (2021), e2107883.
[63] B. Qiao, Y. Luo, H.-B. Cheng, J. Ren, J. Cao, C. Yang, B. Liang, A. Yang, X. Yuan, J. Li, L. Deng, P. Li, H.-T. Ran, L. Hao, Z. Zhou, M. Li, Y. Zhang, P.S. Timashev, X.-J. Liang, Z. Wang, Artificial nanotargeted cells with stable photothermal performance for multimodal imaging-guided tumor-specific therapy, ACS Nano 14 (2020) 12652–12667.
[64] Y. Wang, K. Zhang, T. Li, A. Maruf, X. Qin, L. Luo, Y. Zhong, J. Qiu, S. McGinty, G. Pontrelli, X. Liao, W. Wu, G. Wang, Macrophage membrane functionalized biomimetic nanoparticles for targeted anti-atherosclerosis applications, Theranostics 11 (2021) 164.
[65] T. Liu, M. Zhang, W. Liu, X. Zeng, X. Song, X. Yang, X. Zhang, J. Feng, Metal ion/tannic acid assembly as a versatile photothermal platform in engineering multimodal nanotheranostics for advanced applications, ACS Nano 12 (2018) 3917–3927.
[66] X. Wang, Y. Mao, C. Sun, Q. Zhao, Y. Gao, S. Wang, A versatile gas-generator promoting drug release and oxygen replenishment for amplifying photodynamic-chemotherapy synergetic anti-tumor effects, Biomaterials 276 (2021), 120985.
[67] C. Li, Y. Zhang, Z. Li, E. Mei, J. Lin, F. Li, C. Chen, X. Qing, L. Hou, L. Xiong, H. Hao, Y. Yang, P. Huang, Light-responsive biodegradable nanorattles for cancer theranostics, Adv. Mater. 30 (2018), 1706150.